Hydroxyapatite Pellets as a Biomimetic Bone Substitute for *in vitro* Study of Osteoclasts

By Harrison Cassidy

A thesis submitted to McGill University in partial fulfillment of the requirements for the degree of:

MASTER OF SCIENCE

Department of Chemistry, Faculty of Science

McGill University

Montréal, Québec, Canada

© Harrison Cassidy, 2020

Abstract

Bone is a complex organ housing a variety of cells. Among these are osteoclasts which are directly responsible for resorption of bone by creating an acidic microenvironment and dissolving the inorganic matrix, maintaining the lightweight nature of bone and acting as a reservoir for several essential ions. Due to difficulties associated with locating and cultivating the cells from bone, osteoclast research has only become mainstream in the last half century. To facilitate osteoclast research, the development of surfaces on which the cells can proliferate has become its own area of research. In experiments that strive to mimic bone, calcium hydroxyapatite is often used as the substrate.

Studies on the composition of bone have illustrated several elements that can bioaccumulate in bone, often through facile exchange of either the calcium or phosphate ions in hydroxyapatite. Additionally, osteoclasts have shown extreme sensitivity to many elements, causing increased or decreased osteoclast proliferation and activity. Recently, rapid tungsten bioaccumulation has been observed in bone. Evidence has been published that solubilized monotungstates of low toxicity are converted *in vivo* to more toxic insoluble polytungstate species.

Herein we present a procedure for hydroxyapatite pellet formation for use as a biomimetic substrate for *in vitro* osteoclast study and uniform integration of tungsten into the pellet for future tungsten toxicity experiments. We have synthesized a pH sensitive BODIPY dye capable of fluorescing in the acidic microenvironment made by osteoclasts for *in vitro* study of live cells. We have obtained 2D X-ray fluorescence of osteoclasts and their resorption pits and are the first to have results suggesting that osteoclasts are responsible for the speciation change of tungsten in bone by measuring the X-ray absorption near edge structure.

Abstrait

L’os est un organe complexe, comprenant une variété de cellules. Parmi celles-ci les ostéoclastes sont directement responsables de la résorption de l’os en créant un microenvironnement acide et en dissolvant la matrice inorganique, maintenant ainsi la nature légère de l’os et agissant comme réservoir d’ions essentiels. Du aux difficultés liées à la localisation et la culture de cellules osseuses, la recherche sur l’ostéoclaste est devenue courante depuis un demi-siècle. Afin de faciliter la recherche sur l’ostéoclaste, le développement de surfaces sur lesquelles les cellules prolifèrent est devenu son propre domaine de recherche. Parmi les expériences qui s’évertuent à imiter l’os, l’hydroxyapatite de calcium est souvent utilisé comme substrat.

Les études sur la composition de l’os ont illustré plusieurs éléments qui peuvent se bioaccumuler dans l’os, souvent à travers un échange facile soit du calcium soit des ions phosphates dans l’hydroxyapatite. De plus, les ostéoclastes montrent une extrême sensibilité à beaucoup d’éléments, entrainant une prolifération et une activité accrue ou réduite des ostéoclastes. Récemment, une bioaccumulation rapide de tungstène a été observée dans l’os. Des preuves démontrant que des monotungstates solubilisés de faible toxicité sont convertis in vivo en polytungstates insolubles plus toxiques ont été publiées.

Nous présentons ici une procédure de formation de pastilles d’hydroxyapatite utilisées comme substrat biomimétique pour l’étude in vitro d’ostéoclastes et l’intégration uniforme de tungstène dans la pastille pour de futures expériences sur la toxicité du tungstène. Nous avons synthétisé un colorant BODIPY sensible au pH capable de fluorescer dans un microenvironnement acide fait par les ostéoclastes pour des études in vivo de cellules vivantes. Nous avons obtenu de la fluorescence à rayons X d’ostéoclastes et de leurs puits de résorption et sommes les premiers à avoir des résultats

suggérant que les ostéoclastes sont responsables du changement de spéciation du tungstène dans l’os en mesurant la spectroscopie de structure près du front d'absorption de rayons X.

Acknowledgements

Thank you, Professor Scott Bohle, for welcoming me into your group. You have supported and encouraged me every step of the way and have fought for me and my success. Thank you for your knowledge, compassion and patience throughout my studies.

I would like to thank the members of the Bohle group; Quentin Gaydon, Benita Kapuku David Kuter, Danae López, Andrew Mack, Cassidy VanderSchee, and Ivor Wharf. Everyone in the group at one time or another has helped me troubleshoot my research and it has been an incredible pleasure to get to know each of you.

Thank you, Hsiang Chou for teaching me so much about your cell work, letting me come into your lab to watch and learn what you do. Thank you for always being available and receptive when I have a random and confusing question or experiment idea.

Thank you, Chantal Marotte for going above and beyond every day. Without you, the department would crumble.

A special thanks to Aya Sakaya for teaching me how to measure fluorescence and being more excited than I was when my dye worked.

Victor Lotocki, thank you for your indispensable advice and being a great DM.

To Julia McCain, thank you for pointing out the reason my first reaction wasn't working was because the paper I was referencing had cited the wrong starting material. Thank you for telling me when I write tungsten-containing, it should be hyphenated. Thank you for everything in-between.

Last and certainly not least, thank you to my parents, Veronica and Leonard, and my sisters Emily and Rosie, who have always wished the best for me and loved me unconditionally.

Contribution of authors

This dissertation includes content by Hsiang Chou regarding osteoclast seeding on tungsten-doped hydroxyapatite, **2.2.12**.

Statement of originality and contribution to knowledge

Live cell work was performed by Hsiang Chou. Tungsten-containing hydroxyapatite pellets and tungsten-doped hydroxyapatite pellets were made in part by Andrew Mack and Cassidy VanderSchee. All work presented in this thesis, with the exception of the above contributions and introductory literature review, is declared by the author to be original scholarship and distinct contributions to knowledge as is mandatory for graduate theses.

Table of contents

Table of figures

Table of Schemes

Table of Tables

Chapter 1

Introduction and Literature Review of Osteoclasts and Tungsten Biochemistry

1.1 History of osteoclast science and their functions

While there are four types of cells residing in bone, the two most commonly studied are osteoblasts and osteoclasts, the cells directly responsible for bone deposition and resorption.[1] Bone resorption by osteoclasts is estimated to occur 40-100 times faster than deposition of material by osteoblasts.[2] Osteoclast science has seen explosive growth in the past fifty years. Though initially discovered and their bone resorption function deduced in 1873, osteoclasts were not studied in an isolated culture until over one hundred years later in 1982 by Zambonin *et al.*[3, 4]

Bones are mostly thought of as the structures which protect our organs and act as a framework for locomotion. However, bones have an equally important metabolic function, as reservoirs for calcium, phosphate and other ions.[5] Osteoblasts are responsible for the deposition of bone and the storage of calcium. Osteoclasts are responsible for resorption and release of calcium into the blood. The importance of calcium in neuromuscular function, signaling though synapses, and proper

development of axons is apparent in individuals who are older or malnourished when resorption can exceed deposition, sacrificing structural integrity in order to maintain bodily functions.[6-8]

The first distinguishing feature of osteoclasts is their size, which results from many smaller osteoclasts coming together to make one multi-nucleated cell that can grow to > 200 μm with finger-like projections of the cytoplasm making up what is termed the ruffled border, **Scheme 1**.[3, 9-11] Prior to resorption of bone, an action ring forms in the ruffled border to make a sealing zone in which the osteoclast secretes acid to dissolve the inorganic matrix. The resorbed material is then pumped out through vesicle-like structures into the plasma membrane of the cell and released into the extracellular space.[11-14] To dissolve the calcium hydroxyapatite of bone a pH of ~4.0 or lower is required.[12] Evidence of the osteoclast actively reducing the pH in the resorption area was first discovered by incubation of osteoclasts in a solution of acridine orange as a fluorescent indicator.[14] At a pH of 3.5 or lower, acridine orange fluoresces under UV light. Another observation from this study was that after incubation in base, the osteoclast was able to reacidify the interface between the bone and the cell, providing a visualization of osteoclast activity without cell death.[14] These observations gave a rough indication of the pH level of a resorbing osteoclast but the mechanisms of acid formation and secretion are still poorly understood.[11, 14]

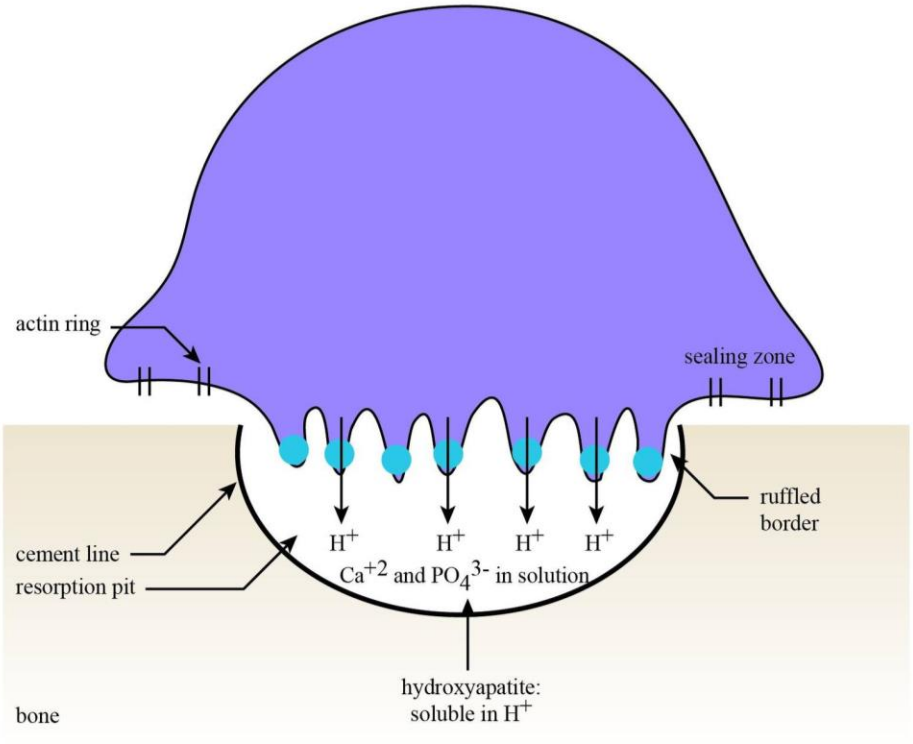

Scheme 1. Simplified diagram of mature osteoclast during resorption.[15]

1.2 Methods of osteoclast study

The most common method of visualizing osteoclasts is staining the enzyme tartrate-resistant acid phosphatase (TRAP). This enzyme has been linked to proper osteoclastic activity, with knockout studies in mice demonstrating increased bone density and deformation, which was attributed to reduced osteoclastic activity.[16] Having been observed in as early a stage of the osteoclast as the single nuclei juveniles, staining for the TRAP enzyme is one of the most common techniques used to identify osteoclasts.[12] In mature osteoclasts, TRAP is localized in the ruffled border, making it easier to differentiate between mature osteoclasts and cells that have newly fused.[12] One disadvantage of TRAP staining is that it results in the death of the osteoclast, so while it has

been invaluable for the study of the identification and morphology of osteoclasts, TRAP staining cannot be used to study live cells.

While it is believed that osteoclast precursors are formed in the bone marrow, the process of osteoclast development *in vivo* is still largely a mystery.[17] RANKL (receptor activator of nuclear factor-κB ligand) is secreted by osteoblasts and binds to osteoclasts and osteoclast precursors, inducing cell-cell fusion and formation of mature osteoclasts.[18] The antithesis to RANKL is OPG (osteoprotegerin), also secreted by osteoblasts, which binds those same osteoclast RANKL receptors, in this case inhibiting cell development.[12] OPG serves as a failsafe to downregulate osteoclastic activity and ensure bone resorption does not go unchecked.[19] Osteoclasts are a relatively uncommon cells and difficult to culture. For *in vitro* studies, precursor cells are often harvested from bone barrow and treated with RANKL to stimulate development.[20]

Early studies of osteoclast activity show increased presence of calcium ions in the extracellular matrix decreases osteoclast activity and therefore the rate of bone resorption.[21] The size, shape, and quantity of resorption pits in a cell culture is used as an indication of osteoclast activity. These can be measured using various microscopic techniques such as confocal and scanning electron microscopy in conjunction with 3D modeling.[22] Osteoclasts have been shown to secrete acid when cultured on plastic dishes, which sparked the development of well plates with mineral coatings to observe the relative activity of osteoclasts.[23, 24] These laminated plastic wells have become the norm for *in vitro* osteoclast study due to their high-throughput nature.[25]

1.3 Biomimetic bone tissue engineering

For studies which seek to use more biomimetic substrates than plastics, it is commonplace to use bone slices.[26, 27] Study of osteoclast resorption depth on bovine bone, synthetic hydroxyapatites and silica glass found resorption was most effective on bovine bone.[28] Sintered bovine bone and hydroxyapatites showed little resorption. Hydroxyapatite in bone, as well as hydroxyapatite synthesized in a lab has a low degree of crystallinity.[29] In order to characterize hydroxyapatite it is sintered at temperatures up to 1250 °C which increases the degree of crystallinity and therefore increases the sharpness of peaks in powder x-ray diffraction. Muralithran *et al.* have shown increasing density of hydroxyapatite with increasing sintering temperatures up to 1250 °C and therefore a reduction of porosity and surface area, **Figure 1**.[30] Osteoblast, and subsequently osteoclast, activity has been shown to be linked to roughness of a surface, where a rougher matrix promotes activity.[27, 31-35] Decreased porosity and surface area as a result of sintering may be the cause of reduced resorption due to insufficient contact of acid and matrix, making the use of sintered hydroxyapatite materials less desirable as a biomimetic bone substitute.

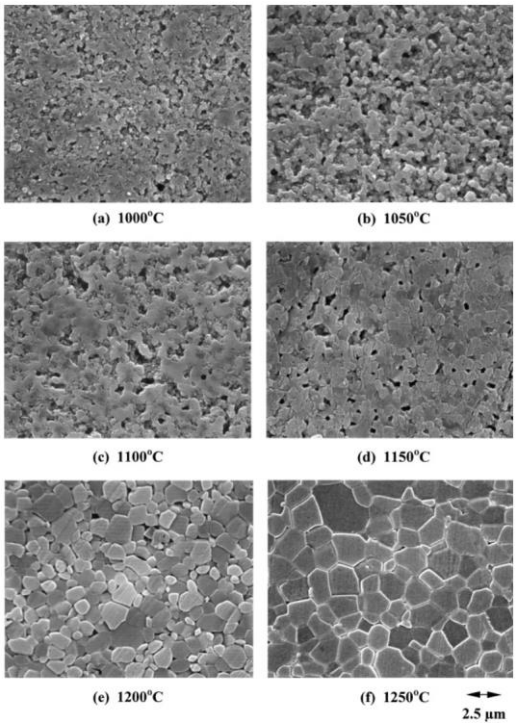

Figure 1. SEM micrographs of polished and etched hydroxyapatite surface sintered at various temperatures. Reprinted with permission from Elsevier: *Ceramics International*, Muralithran, G., Ramesh, S., **2000,** *26* (2), 221-230.[30]

Development of biomimetic bone substates has been driven largely by dentin implants and bone grafts.[29, 36-38] Early synthetic bone attempts revolved around the use of calcium hydroxyapatite, the main inorganic component of bone. It was quickly discovered that while solid grafts provided the greatest support at the time of the graft, after six weeks the graft was more likely to fragment during the resorption process and fracture compared to vascularized substrates.[39-41] To vascularize hydroxyapatite, the powder was typically mixed with hydrogen peroxide to form bubbles, then sintered.[42] One limitation of this technique is that it is almost impossible to control the pore size. Hulbert *et al*. report a minimum pore size of 45-100 μm for a successful vascularization of the graft, with improved outcomes with a pore size in the 100-150 μm range.[43] Use of grafts vascularized before implantation more closely resembles the natural structure of bone and skips the need for revascularization as seen in the solid grafts, resulting in faster incorporation of the

graft into the bone matrix and greater stability after the six week mark.[39] As osteoblasts use collagen as a scaffold for hydroxyapatite precipitation, researchers have used this as well. Collagen in 0.3 mM phosphoric acid has been used to promote fibrillogenesis, development of fine collagen fibrils, to which a solution of calcium hydroxide is added.[44-46] The fine collagen fibrils act as a nucleation site for the hydroxyapatite nanocrystals form uniaxially along the fibril. Wang *et al.* report achieving a 25:75 hydroxyapatite:collagen mixture that, while it does not match the 70:30 ratio *in vivo*, achieves an average pore size of 69.4 μm making it suitable for osteoclast vascularization.[44] Other materials have been tested as a replacement to the collagen in synthetic bone, many of which are polysaccharides such as chitin and alginate, and some groups are using novel scaffolds such as carbon nanotubes.[47, 48] Integration of porous 3D structures is ideal in implantations so osteoclasts can more easily vascularize the material, allowing osteoblasts to build on and strengthen the implant. Because 3D structures for the use of osteoclast study are time consuming, the use of higher throughput 2D matrices is prevalent.[49]

1.4 *In vivo* study of osteoclasts

Conventional methods of fluorescence microscopy including water or oil immersion typically have a working penetration depth of 60 μm into tissue, which has made *in vivo* examination of osteoclasts impractical.[50] Development of two-photon microscopy has allowed for use of near-IR light allowing for increased penetration depths in living tissue up to 2 mm.[50-53] Two-photon excitation requires a fluorophore to be excited by two photons simultaneously, requiring a tight focal point for sufficient probability of excitement.[50] Using two-photon excitation, osteoclasts in mice have been visualized using tdTomato, an enhanced cyan fluorescent protein, and pH sensitive BODIPY dyes.[54] While multiphoton microscopy has been invaluable in bone research, the

equipment availability is low, bottlenecking the number of groups able to effectively research *in vivo* interactions.[54]

1.5 Components of bone

Bone typically comprises approximately 30% organic and 70% inorganic components by dry weight.[55] The organic component of bone is ~90% type I collagen and the inorganic component consists of predominantly hydroxyapatite ($Ca_{10}(PO_4)_6(OH)_2$) where 90% of inorganic material, by molar equivalents, are calcium and phosphate.[56, 57] While these values are generally applicable, the exact proportions can be variable depending on which bone is being studied, whether the section of the bone is cortical or trabecular, and the age and exposure history of the sample's donor. Because of this, the expected 10/6 (1.67) ratio of calcium to phosphate in hydroxyapatite is observed as a range from 1.3 to 2.0.[58] When carbonate, magnesium and sodium are also considered, ≥ 98% of the inorganic matrix is accounted for.[57] By weight, approximately 7.4% of hydroxyapatite in bone exists naturally as carbonated hydroxyapatite, in which a phosphate group or occasionally a hydroxyl is replaced by carbonate, accounting for increased Ca:P ratios from the expected 1.67.[59] Similarly, magnesium and sodium have both been shown to replace the calcium in hydroxyapatite.[59-61] The majority of research on the chemical composition of bone, when performed on human bone, is skewed towards the elderly population, often on femurs following hip replacements due to osteoporosis which is not representative of healthy bone, but gives valuable information on bioaccumulation in bone.[56, 62-67]

Several cations have been shown to coordinate to hydroxyapatite, including strontium, lead and mercury.[58, 68] **Table 1** shows a handful of reports which examine the elements found in bone and

demonstrates the wide range of elements that are either naturally present or bioaccumulate. The elements in **Table 1** are not an exhaustive list of the elements that have been observed in bone.

Table 1. Reports summarizing elementals found in bone. Reviews which discuss downstream effects are marked with *****.

Source	Elements Found in Bone
Review of Metal Exposure and Its Effects on Bone Health* [56]	Cd, Ni, Hg, Cr, Pb, Al, Ti, Fe, As
Metals in Bone: Aluminum, Boron, Cadmium, Chromium, Lanthanum, Lead, Silicon, and Strontium* [62]	Al, Cr, La, Pb, Si, St
Concentration of Bone Elements in Osteoporosis [63]	Na, K, Mg, Cu, Zn, Fe, Sr, Al, B, Si, F, Pb
Concentrations of Selected Heavy Metals in Bones and Femoral Bone Structure of Bank (Myodes glareolus) and Common (Microtus arvalis) Voles from Different Polluted Biotopes in Slovakia [64]	Pb, Cd, Ni, Fe, Cu, Zn
Determination of 14 Elements in Taiwanese Bones [65]	As, Zn, Cd, Pb, Ni, Co, Mn, Fe, Cr, Mg, Al, Cu, Ag, Ca
Elemental Analysis of Femoral Bone From Patients With Fractured Neck of Femur or Osteoarthrosis [66]	Ca, P, Mg, Na, Al, B, Ba, Fe, K, Pb, St, Sn, Zn
An Assessment of Natural Concentrations of Selected Metals in the Bone Tissues of the Femur Head [67]	Fe, K, Cd, Cu, Pb

1.6 Osteoclast response to stimuli

Bioaccumulation of many of the elements in **Table 1** has been shown to have a measurable impact on osteoclast proliferation and activity. Aluminum for example, is resorbed by osteoclasts and deposited on trabecular bone, which has been linked to a number of bone diseases.[56] Chromium(III) at 0.1 µM has been shown to stimulate osteoclast development and resorption by up to 200% and 300%, respectively.[69] Cobalt(II) has been linked to increased osteoclast formation

and resorption and is suspected to increase osteolysis and loosening of bone implants.[70] Conversely, zinc has been linked to a decrease in osteoclast activity at concentrations as low as 10^{-14} M, but showed no significant decrease in osteoclast proliferation at any of the measured concentrations, up to 10^{-4} M.[71, 72] Strontium-containing bioceramics have been shown to decrease osteoclast development, whereas silica enhances osteoclast activity.[20] Magnesium hydroxide has been shown to reduce osteoclasts activity while simultaneously increase osteoblast differentiation.[73] Another study finds titanium, aluminum, gold, iron and vanadium all decrease the total number of multinucleated osteoclasts.[74] The study of osteoclasts and their response to various stimuli is a quickly emerging area of research with many interactions that have yet to be sufficiently investigated. One such interaction is bioaccumulation of tungsten.

1.7 Biochemistry of tungsten

Tungsten has been shown to have biological significance in prokaryotes but with no known role in eukaryotes.[75] It is generally believed that through evolution tungsten-containing enzymes have been replaced in favor of molybdenum.[75] Initial toxicological studies of tungsten used monotungstate salts and found that tungsten is a relatively inert metal with low toxicity.[76-80] Due to tungsten being deemed non-toxic and its impressive physical properties, tungsten-containing compounds have become an integral component of society.[78, 81] Poor disposal of tungsten-containing products and wear and tear of tungsten carbine studded tires during winter months may lead to increased tungsten concentration in soil. It has been suggested by Strigul *et al*. that metallic tungsten in soil can have negative effects on plant life and microbes in the soil.[82-85]

In recent years, the toxicity of polytungstates has been called into question with experiments showing sodium metatungstate ($Na_6[H_2W_{12}O_{40}]$) having significantly higher taxological effects than sodium tungstate (Na_2WO_4).[86] There have been three acute childhood leukemia outbreaks from 1997 to 2003 recorded near naturally occurring tungsten deposits, refineries and/or military bases.[78, 87-89] Tungsten ingested by mice in the soluble form of Na_2WO_4 has been shown to accumulate in bone and persist after exposure.[90] Chelation therapy which has been shown to effectively remove lead, and strontium, is ineffectual in the removal of tungsten.[91-95] These results have led to reexamination of tungsten toxicological effects and whether other tungstates are toxic and a call to determine which forms of tungsten exist in the environment, and which interconversions they undergo in physiological conditions.[96]

1.8 Outlook of future research

Our understanding of osteoclasts has improved significantly in the past few decades. What is clear is that osteoclasts are profoundly affected by the ions in their environment. It is critical to study the interactions of osteoclasts with solutes that diffuse through the blood into bone. Although two-photon excitation of fluorescent probes will be key for *in vivo* studies of many of these complex interactions, *in vitro* studies will continue to be key in controlling experimental conditions to pinpoint osteoclast response to stimuli. In order to maximize the effectiveness of *in vitro* studies, research is required into both substrates that are more biomimetic and improved methods for visualization of live cells. In this thesis, procedures for hydroxyapatite pellet formation and incorporation of doping elements is refined. Additionally, pH sensitive fluorescent methods for visualization of osteoclast activity are investigated.

1.9 References

1. Florencio-Silva, R.; Sasso, G. R. d. S.; Sasso-Cerri, E.; Simões, M. J.; Cerri, P. S., Biology of Bone Tissue: Structure, Function, and Factors That Influence Bone Cells. *BioMed Research International* **2015,** *2015*, 421746.
2. Cooper, D. M. L.; Erickson, B.; Peele, A. G.; Hannah, K.; Thomas, C. D. L.; Clement, J. G., Visualization of 3D osteon morphology by synchrotron radiation micro-CT. *Journal of Anatomy* **2011,** *219* (4), 481-489.
3. Martin, T. J., Historically significant events in the discovery of RANK/RANKL/OPG. *World J Orthop* **2013,** *4* (4), 186-197.
4. Zambonin Zallone, A.; Teti, A.; Primavera, M. V., Isolated osteoclasts in primary culture: first observations on structure and survival in culture media. *Anat Embryol (Berl)* **1982,** *165* (3), 405-13.
5. Mohamed, A. M., An overview of bone cells and their regulating factors of differentiation. *Malays J Med Sci* **2008,** *15* (1), 4-12.
6. Becerikli, M.; Jaurich, H.; Schira, J.; Schulte, M.; Döbele, C.; Wallner, C.; Abraham, S.; Wagner, J. M.; Dadras, M.; Kneser, U.; Lehnhardt, M.; Behr, B., Age-dependent alterations in osteoblast and osteoclast activity in human cancellous bone. *J Cell Mol Med* **2017,** *21* (11), 2773-2781.
7. Katz, B., The role of calcium in neuromuscular facilitation. *Journal of Physiology, The* **1968,** *195* (2), 481.
8. Tessier, C. R., Considering calcium-binding proteins in invertebrates: multi-functional proteins that shape neuronal growth. *Neural Regen Res* **2016,** *11* (2), 208-209.
9. Holtrop, M. E.; King, G. J., The ultrastructure of the osteoclast and its functional implications. *Clin Orthop Relat Res* **1977,** (123), 177-96.
10. Roodman, G. D., Advances in bone biology: the osteoclast. *Endocrine Reviews* **1996,** *17* (4), 308.
11. Czupalla, C.; Mansukoski, H.; Riedl, T.; Thiel, D.; Krause, E.; Hoflack, B., Proteomic Analysis of Lysosomal Acid Hydrolases Secreted by Osteoclasts. *Molecular & Cellular Proteomics* **2006,** *5* (1), 134.
12. Detsch, R.; Boccaccini, A. R., The role of osteoclasts in bone tissue engineering. *Journal of Tissue Engineering and Regenerative Medicine* **2015,** *9* (10), 1133-1149.
13. Anderegg, F.; Geblinger, D.; Horvath, P.; Charnley, M.; Textor, M.; Addadi, L.; Geiger, B., Substrate adhesion regulates sealing zone architecture and dynamics in cultured osteoclasts. *PLoS One* **2011,** *6* (12), e28583-e28583.
14. Baron, R.; Neff, L.; Louvard, D.; Courtoy, P. J., Cell-mediated extracellular acidification and bone resorption: evidence for a low pH in resorbing lacunae and localization of a 100-kD lysosomal membrane protein at the osteoclast ruffled border. *Journal of Cell Biology* **1985,** *101* (6), 2210-2222.
15. Qureshi, S., The Young Orthopod. 2017; Vol. 2018.
16. Hayman, A. R.; Jones, S. J.; Boyde, A.; Foster, D.; Colledge, W. H.; Carlton, M. B.; Evans, M. J.; Cox, T. M., Mice lacking tartrate-resistant acid phosphatase (Acp 5) have disrupted endochondral ossification and mild osteopetrosis. *Development* **1996,** *122* (10), 3151-62.
17. Ikeda, K.; Takeshita, S., The role of osteoclast differentiation and function in skeletal homeostasis. *The Journal of Biochemistry* **2015,** *159* (1), 1-8.

18. Kearns, A. E.; Khosla, S.; Kostenuik, P. J., Receptor activator of nuclear factor kappaB ligand and osteoprotegerin regulation of bone remodeling in health and disease. *Endocrine reviews* **2008,** *29* (2), 155-192.
19. Boyce, B. F.; Xing, L., The RANKL/RANK/OPG pathway. *Curr Osteoporos Rep* **2007,** *5* (3), 98-104.
20. Steffi, C.; Shi, Z.; Kong, C. H.; Wang, W., Modulation of Osteoclast Interactions with Orthopaedic Biomaterials. *J Funct Biomater* **2018,** *9* (1), 18.
21. Zaidi, M.; Kerby, J.; Huang, C. L.; Alam, T.; Rathod, H.; Chambers, T. J.; Moonga, B. S., Divalent cations mimic the inhibitory effect of extracellular ionised calcium on bone resorption by isolated rat osteoclasts: further evidence for a "calcium receptor". *J Cell Physiol* **1991,** *149* (3), 422-7.
22. Goldberg, S. R.; Georgiou, J.; Glogauer, M.; Grynpas, M. D., A 3D scanning confocal imaging method measures pit volume and captures the role of Rac in osteoclast function. *Bone* **2012,** *51* (1), 145-152.
23. Rao, H.; Tan, J.; Faruqi, F.; Beltzer, J., Corning® Osteo Assay Surface: A New Tool to Study Osteoclast and Osteoblast Differentiation and Function. Corning Incorporated Sullivan Park, NY 14831: 2011.
24. Takahashi, N.; Ejiri, S.; Yanagisawa, S.; Ozawa, H., Regulation of osteoclast polarization. *Odontology* **2007,** *95* (1), 1-9.
25. Diepenhorst, N. A.; Nowell, C. J.; Rueda, P.; Henriksen, K.; Pierce, T.; Cook, A. E.; Pastoureau, P.; Sabatini, M.; Charman, W. N.; Christopoulos, A.; Summers, R. J.; Sexton, P. M.; Langmead, C. J., High throughput, quantitative analysis of human osteoclast differentiation and activity. *Analytical Biochemistry* **2017,** *519*, 51-56.
26. ARNETT, T. R.; DEMPSTER, D. W., Effect of pH on Bone Resorption by Rat Osteoclasts in Vitro. *Endocrinology* **1986,** *119* (1), 119-124.
27. Matsunaga, T.; Inoue, H.; Kojo, T.; Hatano, K.; Tsujisawa, T.; Uchiyama, C.; Uchida, Y., Disaggregated osteoclasts increase in resorption activity in response to roughness of bone surface. *Journal of Biomedical Materials Research* **1999,** *48* (4), 417-423.
28. Taylor, J. C.; Cuff, S. E.; Leger, J. P.; Morra, A.; Anderson, G. I., In vitro osteoclast resorption of bone substitute biomaterials used for implant site augmentation: a pilot study. *Int J Oral Maxillofac Implants* **2002,** *17* (3), 321-30.
29. Liao, S. S.; Cui, F. Z.; Zhang, W.; Feng, Q. L., Hierarchically biomimetic bone scaffold materials: Nano-HA/collagen/PLA composite. *Journal of Biomedical Materials Research Part B: Applied Biomaterials* **2004,** *69B* (2), 158-165.
30. Muralithran, G.; Ramesh, S., The effects of sintering temperature on the properties of hydroxyapatite. *Ceramics International* **2000,** *26* (2), 221-230.
31. Chehroudi, B. The effects of surface topography on the behaviour of cells attached to percutaneous implants. Text, 1991.
32. Chehroudi, B.; Ratkay, J.; Brunette, D., The role of implant surface geometry on mineralization in vivo and in vitro: A transmission and scanning electron microscopic study. *Cells Mater* **1992,** *2*, 89-104.
33. Martin, J. Y.; Schwartz, Z.; Hummert, T. W.; Schraub, D. M.; Simpson, J.; Lankford Jr., J.; Dean, D. D.; Cochran, D. L.; Boyan, B. D., Effect of titanium surface roughness on proliferation, differentiation, and protein synthesis of human osteoblast-like cells (MG63). *Journal of Biomedical Materials Research* **1995,** *29* (3), 389-401.

34. Boyan, B. D.; Lossdörfer, S.; Wang, L.; Zhao, G.; Lohmann, C. H.; Cochran, D. L.; Schwartz, Z., Osteoblasts generate an osteogenic microenvironment when grown on surfaces with rough microtopographies. *Eur Cell Mater* **2003,** *6*, 22-7.
35. Boyan, B. D.; Lotz, E. M.; Schwartz, Z., (*) Roughness and Hydrophilicity as Osteogenic Biomimetic Surface Properties. *Tissue Eng Part A* **2017,** *23* (23-24), 1479-1489.
36. Mehta, M.; Schmidt-Bleek, K.; Duda, G. N.; Mooney, D. J., Biomaterial delivery of morphogens to mimic the natural healing cascade in bone. *Advanced Drug Delivery Reviews* **2012,** *64* (12), 1257-1276.
37. Meyer, U.; Joos, U.; Wiesmann, H. P., Biological and biophysical principles in extracorporal bone tissue engineering: Part I. *International Journal of Oral and Maxillofacial Surgery* **2004,** *33* (4), 325-332.
38. Ciapetti, G.; Di Pompo, G.; Avnet, S.; Martini, D.; Diez-Escudero, A.; Montufar, E. B.; Ginebra, M.-P.; Baldini, N., Osteoclast differentiation from human blood precursors on biomimetic calcium-phosphate substrates. *Acta Biomaterialia* **2017,** *50*, 102-113.
39. Zimmermann, G.; Moghaddam, A., Allograft bone matrix versus synthetic bone graft substitutes. *Injury* **2011,** *42*, S16-S21.
40. Grenga, T. E.; Zins, J. E.; Bauer, T. W., The rate of vascularization of coralline hydroxyapatite. *Plast Reconstr Surg* **1989,** *84* (2), 245-249.
41. Dell, P. C.; Burchardt, H.; Glowczewskie, F. P., Jr., A roentgenographic, biomechanical, and histological evaluation of vascularized and non-vascularized segmental fibular canine autografts. *JBJS* **1985,** *67* (1).
42. Moore, W. R.; Graves, S. E.; Bain, G. I., Synthetic bone graft substitutes. *ANZ Journal of Surgery* **2001,** *71* (6), 354-361.
43. Hulbert, S. F.; Morrison, S. J.; Klawitter, J. J., Tissue reaction to three ceramics of porous and non-porous structures. *Journal of Biomedical Materials Research* **1972,** *6* (5), 347-374.
44. Wang, J.; Liu, C., Biomimetic Collagen/Hydroxyapatite Composite Scaffolds: Fabrication and Characterizations. *Journal of Bionic Engineering* **2014,** *11* (4), 600-609.
45. Uquillas, J. A.; Kishore, V.; Akkus, O., Effects of phosphate-buffered saline concentration and incubation time on the mechanical and structural properties of electrochemically aligned collagen threads. *Biomed Mater* **2011,** *6* (3), 035008-035008.
46. Kikuchi, M.; Ikoma, T.; Itoh, S.; Matsumoto, H. N.; Koyama, Y.; Takakuda, K.; Shinomiya, K.; Tanaka, J., Biomimetic synthesis of bone-like nanocomposites using the self-organization mechanism of hydroxyapatite and collagen. *Composites Science and Technology* **2004,** *64* (6), 819-825.
47. Zhao, B.; Hu, H.; Mandal, S. K.; Haddon, R. C., A Bone Mimic Based on the Self-Assembly of Hydroxyapatite on Chemically Functionalized Single-Walled Carbon Nanotubes. *Chemistry of Materials* **2005,** *17* (12), 3235-3241.
48. Venkatesan, J.; Bhatnagar, I.; Manivasagan, P.; Kang, K.-H.; Kim, S.-K., Alginate composites for bone tissue engineering: A review. *International Journal of Biological Macromolecules* **2015,** *72*, 269-281.
49. Sieberath, A.; Della Bella, E.; Ferreira, A. M.; Gentile, P.; Eglin, D.; Dalgarno, K., A Comparison of Osteoblast and Osteoclast In Vitro Co-Culture Models and Their Translation for Preclinical Drug Testing Applications. *Int. J. Mol. Sci.* **2020,** *21*, 912.
50. Cahalan, M. D.; Parker, I.; Wei, S. H.; Miller, M. J., Two-photon tissue imaging: seeing the immune system in a fresh light. *Nature Reviews Immunology* **2002,** *2* (11), 872-880.

51. Germain, R. N.; Miller, M. J.; Dustin, M. L.; Nussenzweig, M. C., Dynamic imaging of the immune system: progress, pitfalls and promise. *Nature Reviews Immunology* **2006,** *6* (7), 497-507.
52. Centonze, V. E.; White, J. G., Multiphoton excitation provides optical sections from deeper within scattering specimens than confocal imaging. *Biophys J* **1998,** *75* (4), 2015-2024.
53. Dong, C. Y.; Yu, B.; Kaplan, P. D.; So, P. T., Performances of high numerical aperture water and oil immersion objective in deep-tissue, multi-photon microscopic imaging of excised human skin. *Microsc Res Tech* **2004,** *63* (1), 81-6.
54. Ishii, M., *Intravital Imaging of Dynamic Bone and Immune Systems: Methods and Protocols*. Springer New York: 2018.
55. Gong, J. K.; Arnold, J. S.; Cohn, S. H., Composition of trabecular and cortical bone. *The Anatomical Record* **1964,** *149* (3), 325-331.
56. Rodríguez, J.; Mandalunis, P. M., A Review of Metal Exposure and Its Effects on Bone Health. *J Toxicol* **2018,** *2018*, 4854152.
57. Burnell, J. M.; Baylink, D. J.; Chestnut, C. H., 3rd; Mathews, M. W.; Teubner, E. J., Bone matrix and mineral abnormalities in postmenopausal osteoporosis. *Metabolism* **1982,** *31* (11), 1113-20.
58. Hall, J. E.; Guyton, A. C., *Pocket Companion to Guyton & Hall Textbook of Medical Physiology*. Elsevier Saunders: 2006.
59. Senra, M. R.; Lima, R. B. d.; Souza, D. d. H. S.; Marques, M. d. F. V.; Monteiro, S. N., Thermal characterization of hydroxyapatite or carbonated hydroxyapatite hybrid composites with distinguished collagens for bone graft. *Journal of Materials Research and Technology* **2020,** *9* (4), 7190-7200.
60. Barrère, F.; van Blitterswijk, C. A.; de Groot, K., Bone regeneration: molecular and cellular interactions with calcium phosphate ceramics. *International Journal of Nanomedicine* **2006,** *1* (3), 317-332.
61. Bose, S.; Tarafder, S., Calcium phosphate ceramic systems in growth factor and drug delivery for bone tissue engineering: A review. *Acta Biomaterialia* **2012,** *8* (4), 1401-1421.
62. Bronner, F., Chapter 25 - Metals in Bone: Aluminum, Boron, Cadmium, Chromium, Lanthanum, Lead, Silicon, and Strontium. In *Principles of Bone Biology (Third Edition)*, Bilezikian, J. P.; Raisz, L. G.; Martin, T. J., Eds. Academic Press: San Diego, 2008; pp 515-531.
63. Baslé, M. F.; Mauras, Y.; Audran, M.; Clochon, P.; Rebel, A.; Allain, P., Concentration of bone elements in osteoporosis. *J Bone Miner Res* **1990,** *5* (1), 41-7.
64. Martiniaková, M.; Omelka, R.; Jančová, A.; Stawarz, R.; Formicki, G., Concentrations of Selected Heavy Metals in Bones and Femoral Bone Structure of Bank (Myodes glareolus) and Common (Microtus arvalis) Voles from Different Polluted Biotopes in Slovakia. *Archives of Environmental Contamination and Toxicology* **2011,** *60* (3), 524-532.
65. Kuo, H. W.; Kuo, S. M.; Chou, C. H.; Lee, T. C., Determination of 14 elements in Taiwanese bones. *Sci Total Environ* **2000,** *255* (1-3), 45-54.
66. Helliwell, T. R.; Kelly, S. A.; Walsh, H. P.; Klenerman, L.; Haines, J.; Clark, R.; Roberts, N. B., Elemental analysis of femoral bone from patients with fractured neck of femur or osteoarthrosis. *Bone* **1996,** *18* (2), 151-7.
67. Wiechuła, D.; Jurkiewicz, A.; Loska, K., An assessment of natural concentrations of selected metals in the bone tissues of the femur head. *Science of The Total Environment* **2008,** *406* (1), 161-167.

68. Sánchez-Chardi, A.; López-Fuster, M. J.; Nadal, J., Bioaccumulation of lead, mercury, and cadmium in the greater white-toothed shrew, Crocidura russula, from the Ebro Delta (NE Spain): Sex- and age-dependent variation. *Environmental Pollution* **2007,** *145* (1), 7-14.
69. Aldabbagh, F., 3.03 - Aldehydes: Aryl and Heteroaryl Aldehydes. In *Comprehensive Organic Functional Group Transformations II*, Katritzky, A. R.; Taylor, R. J. K., Eds. Elsevier: Oxford, 2005; pp 99-133.
70. Patntirapong, S.; Habibovic, P.; Hauschka, P. V., Effects of soluble cobalt and cobalt incorporated into calcium phosphate layers on osteoclast differentiation and activation. *Biomaterials* **2009,** *30* (4), 548-555.
71. Moonga, B. S.; Dempster, D. W., Zinc is a potent inhibitor of osteoclastic bone resorption in vitro. *Journal of Bone and Mineral Research* **1995,** *10* (3), 453-457.
72. Yamaguchi, M., Role of nutritional zinc in the prevention of osteoporosis. *Mol Cell Biochem* **2010,** *338* (1-2), 241-54.
73. Janning, C.; Willbold, E.; Vogt, C.; Nellesen, J.; Meyer-Lindenberg, A.; Windhagen, H.; Thorey, F.; Witte, F., Magnesium hydroxide temporarily enhancing osteoblast activity and decreasing the osteoclast number in peri-implant bone remodelling. *Acta Biomaterialia* **2010,** *6* (5), 1861-1868.
74. Rousselle, A. V.; Heymann, D.; Demais, V.; Charrier, C.; Passuti, N.; Baslé, M. F., Influence of metal ion solutions on rabbit osteoclast activities in vitro. *Histol Histopathol* **2002,** *17* (4), 1025-32.
75. Bevers, L. E.; Hagedoorn, P.-L.; Hagen, W. R., The bioinorganic chemistry of tungsten. *Coordination Chemistry Reviews* **2009,** *253* (3), 269-290.
76. Bowen, H. J. M., *Trace elements in biochemistry*. London, New York: Academic Press: 1966; p 241 pp.
77. Wood, J. M., Biological Cycles for Toxic Elements in the Environment. *Science* **1974,** *183* (4129), 1049-1052.
78. Koutsospyros, A.; Braida, W.; Christodoulatos, C.; Dermatas, D.; Strigul, N., A review of tungsten: From environmental obscurity to scrutiny. *Journal of Hazardous Materials* **2006,** *136* (1), 1-19.
79. Clausen, J. L.; Korte, N., Environmental fate of tungsten from military use. *Science of The Total Environment* **2009,** *407* (8), 2887-2893.
80. Strigul, N., Does speciation matter for tungsten ecotoxicology? *Ecotoxicology and Environmental Safety* **2010,** *73* (6), 1099-1113.
81. Shah Idil, A.; Donaldson, N., The use of tungsten as a chronically implanted material. *Journal of Neural Engineering* **2018,** *15* (2), 021006.
82. Strigul, N.; Koutsospyros, A.; Arienti, P.; Christodoulatos, C.; Dermatas, D.; Braida, W., Effects of tungsten on environmental systems. *Chemosphere* **2005,** *61* (2), 248-258.
83. Johnson, D. R.; Inouye, L. S.; Bednar, A. J.; Clarke, J. U.; Winfield, L. E.; Boyd, R. E.; Ang, C. Y.; Goss, J., Tungsten bioavailability and toxicity in sunflowers (Helianthus annuus L.). *Land Contamination & Reclamation* **2009,** *17* (1), 141-151.
84. Sadiq, M.; Mian, A. A.; AlThagafi, K. M., Inter-city comparison of metals in scalp hair collected after the gulf war 1991. *Journal of Environmental Science and Health . Part A: Environmental Science and Engineering and Toxicology* **1992,** *27* (6), 1415-1431.
85. Bäckström, M.; Nilsson, U.; Håkansson, K.; Allard, B.; Karlsson, S., Speciation of Heavy Metals in Road Runoff and Roadside Total Deposition. *Water, Air, and Soil Pollution* **2003,** *147* (1), 343-366.

86. Strigul, N.; Koutsospyros, A.; Christodoulatos, C., Tungsten speciation and toxicity: Acute toxicity of mono- and poly-tungstates to fish. *Ecotoxicology and Environmental Safety* **2010,** *73* (2), 164-171.
87. Bednar, A. J.; Jones, W. T.; Boyd, R. E.; Ringelberg, D. B.; Larson, S. L., Geochemical Parameters Influencing Tungsten Mobility in Soils. *Journal of Environmental Quality* **2008,** *37* (1), 229-233.
88. Rubin, C. S.; Holmes, A. K.; Belson, M. G.; Jones, R. L.; Flanders, W. D.; Kieszak, S. M.; Osterloh, J.; Luber, G. E.; Blount, B. C.; Barr, D. B.; Steinberg, K. K.; Satten, G. A.; McGeehin, M. A.; Todd, R. L., Investigating Childhood Leukemia in Churchill County, Nevada. *Environmental Health Perspectives* **2007,** *115* (1), 151-157.
89. Seiler, R. L.; Stollenwerk, K. G.; Garbarino, J. R., Factors controlling tungsten concentrations in ground water, Carson Desert, Nevada. *Applied Geochemistry* **2005,** *20* (2), 423-441.
90. Guandalini, G. S.; Zhang, L.; Fornero, E.; Centeno, J. A.; Mokashi, V. P.; Ortiz, P. A.; Stockelman, M. D.; Osterburg, A. R.; Chapman, G. G., Tissue Distribution of Tungsten in Mice Following Oral Exposure to Sodium Tungstate. *Chemical Research in Toxicology* **2011,** *24* (4), 488-493.
91. VanderSchee, C. R.; Kuter, D.; Bolt, A. M.; Lo, F.-C.; Feng, R.; Thieme, J.; Chen-Wiegart, Y.-c. K.; Williams, G.; Mann, K. K.; Bohle, D. S., Accumulation of persistent tungsten in bone as in situ generated polytungstate. *Communications Chemistry* **2018,** *1* (1), 8.
92. Bolt, A. M.; Sabourin, V.; Molina, M. F.; Police, A. M.; Negro Silva, L. F.; Plourde, D.; Lemaire, M.; Ursini-Siegel, J.; Mann, K. K., Tungsten targets the tumor microenvironment to enhance breast cancer metastasis. *Toxicol Sci* **2015,** *143* (1), 165-77.
93. Bolt, A. M.; Sabourin, V.; Molina, M. F.; Police, A. M.; Negro Silva, L. F.; Plourde, D.; Lemaire, M.; Ursini-Siegel, J.; Mann, K. K., Tungsten Targets the Tumor Microenvironment to Enhance Breast Cancer Metastasis. *Toxicological Sciences* **2014,** *143* (1), 165-177.
94. Pemmer, B.; Roschger, A.; Wastl, A.; Hofstaetter, J. G.; Wobrauschek, P.; Simon, R.; Thaler, H. W.; Roschger, P.; Klaushofer, K.; Streli, C., Spatial distribution of the trace elements zinc, strontium and lead in human bone tissue. *Bone* **2013,** *57* (1), 184-193.
95. Kelly, A. D. R.; Lemaire, M.; Young, Y. K.; Eustache, J. H.; Guilbert, C.; Molina, M. F.; Mann, K. K., In Vivo Tungsten Exposure Alters B-Cell Development and Increases DNA Damage in Murine Bone Marrow. *Toxicological Sciences* **2012,** *131* (2), 434-446.
96. Lemus, R.; Venezia, C. F., An update to the toxicological profile for water-soluble and sparingly soluble tungsten substances. *Crit Rev Toxicol* **2015,** *45* (5), 388-411.

Chapter 2

Biomimetic Bone Substrates

2.1 Introduction

While there are four types of cells residing in bone, the two most commonly studied are osteoblasts and osteoclasts, the cells directly responsible for bone deposition and resorption, respectively.[1] Due to difficulties accessing and viewing the cells *in vivo*, in addition to species specific differences in bone, the majority of studies on osteoblasts and osteoclasts are done *in vitro*.[2] One of the most common methods of study which offers the highest throughput involves seeding cells on well plates, such as Corning® Osteo Assay Surface.[3] Osteoclast resorption pits have been observed on such plastics with studies referring to changes in total pit number and average diameter in a response to protein stimuli of osteoclasts.[4] Studies such as these give good indications of the relative effects on osteoclast response to stimuli, however, the use of a substrate which more closely mimics bone is likely to better replicate *in vivo* osteoclast behaviours.

Conversely, use of real bone slices has its own limitations including low throughput, difficulty to obtain human samples, minute differences in bone composition between species and inconsistencies in samples from one subject to another.[2, 5] Use of materials designed to mimic bone offers a middle ground with minimal impact to throughput, increased consistency in samples with the ability to adjust the sample to mimic various bone types, with the added benefit of using fewer animal samples. One alteration that could be made to the bone mimic is addition of elements or compounds, such as lead or strontium, to simulate bioaccumulation and bypass the time required for accumulation in animal samples.

Materials to mimic bone is a growing research area for use in bone grafts as they are among the most common surgical procedures worldwide.[6] Early synthetic bone attempts revolved around the use of calcium hydroxyapatite, the main mineral found in bone. Efforts have also been made to make bone mimics more bone like, mimicking not only the inorganic component, but also the organic component, often using collagen itself to serve as a nucleation site for hydroxyapatite and serve to strengthen the end product when under tension.[7, 8] Materials for bone grafts have since moved away from bioinert materials which most closely mimic bone, to bioactive materials similar to bone in physical properties with growth factors to help stimulate cell development.[6, 8-10] While synthetic bone has moved from mimicking bone as closely as possible to bioactive materials, bioinert materials that more closely resemble bone serve as useful substrates for the study of osteoclast function.

This chapter focuses on the development of biomimetic bone substitutes in the form of hydroxyapatite pellets; as a substrate to study osteoclast activity *in vitro*. We will discuss the integration of tungsten into pellets with the aim of obtaining homogeneous dispersion and incorporation of a variety of tungstate species. The incorporation of tungsten into such pellets is

of interest due three acute childhood leukemia outbreaks all near naturally occurring tungsten deposits, refineries and/or military bases and an observation by *Guandalini et al.* that tungsten accumulation in mice occurs primarily in bone.[11-15] Lastly, we will discuss preliminary results of visualization of osteoclast pit formation and modification of tungsten speciation.

2.2 Materials and methods

2.2.1 Pellet pressing

Pellets were pressed using a 30-ton press from "Research & Industrial Instrument Company London England". Pellets were pressed in an 8-mm Diameter ID Hardened Steel Dry Pressing Die Set from Across International. Pressure was estimated using the ½ inch gauge on the press. Milling was performed with a Retsch Mixer Mill MM400 and 15 mL zirconium jars.

2.2.2 Laser ICP-MS

Laser ICP-MS was performed using a Thermo Finnigan iCapQ ICP-MS and deconvoluted using Qtegra version 2.8.3170.392.

2.2.3 XRF

SR-μXRF measurements on the VESPERS beamline at Canadian Light Source (CLS) in Saskatchewan, Canada were performed using the polychromatic incident beam ("pink beam" mode), which covered the energy range of 5–30 keV and with a slit size of 0.1 x 0.1 mm.

2.2.4 XANES

X-ray absorption experiments were carried out at beamline 20 ID in The Advanced Photon Source (APS) in Illinois, USA. Data was processed using 2D Qscan Plot v5.0.0.11. The APD 20-ID uses an Si(111) monochromator with an energy range of 4.3-27 keV and resolution ($\Delta E/E$) of $1.4 \cdot 10^{-4}$. The flux is $1 \cdot 10^{12}$ and beam size when focused is 5 µm x 5 µm.

2.2.5 Preparation of biomimetic bone mimic pellets

Between 45-50 mg hydroxyapatite powder from Sigma-Aldrich were weighed on an electric balance and set aside. The first of two dye anvils was wiped clean and placed carefully into the sleeve and pushed down to the support plate with the piston. Using a pipette one drop of ethanol was added to the anvil and was spread by inserting and lightly spinning the piston. The piston was wiped dry. The sample of hydroxyapatite was carefully poured from the weigh paper to the die. The die was lightly tapped to even out the powder. The piston was inserted and lightly spun to create a flat and even surface. A drop of ethanol was added to the second anvil and spread. A Kimwipe was used to wick away most of the ethanol. The second anvil was placed in the sleeve, ethanol side down, and lightly pressed down with the piston.

The die was placed on the press and the pressure was raised to ~10 tons according to the ½ inch gauge (approximately 25 tons total) and pressure maintained for about half a minute, increasing the pressure slightly whenever the pressure dropped below the 10-ton mark. The pressure was then released, the die carefully removed, inverted, the support plate removed and replaced by the pellet ejector. The die was placed back onto the press and the base of the press raised to move the anvils out of the sleeve. Little to no pressure was used. The press was operated with one hand and the die

supported by the other, ensuring the sleeve did not come down too hard. When the first anvil and pellet had made their way out of the sleeve, the die was removed from the press, the pellet ejector removed, and the first anvil carefully lifted from the pellet. The pellet was slid off the second anvil, using tweezers as a guide. The pellets were left to air dry so any ethanol may evaporate. Between samples, the die was washed with water followed by ethanol.

For easier handling, a small strip (~1 mm in width) of Kapton tape was cut, half of the strip was placed on the back of the pellet and the other half folded onto itself making a small tab.

2.2.6 Incorporation of collagen into a hydroxyapatite pellet

Collagen and hydroxyapatite were mixed in a ratio of 70:30 by mass, roughly mimicking the composition of bone.[16] Collagen was milled in 15 mL zirconium jars filled to ⅓ capacity followed by two 7 mm balls per jar. The samples were milled for 30 minutes at a frequency of 760 min^{-1}. For a 50 mg pellet, 15 mg powdered collagen was mixed with 35 mg hydroxyapatite using a pestle and mortar before being pressed into a pellet, following the above procedure.

2.2.7 Use of lubricant in pellet formation

In a subsequent experiment, ethanol was replaced with a small amount of Nujol oil. One drop of oil was added to each anvil and using a Kimwipe, the majority of oil was wicked away, leaving a thin coating. Following ejection, the pellet was placed in a petri dish and, with a wash bottle, each side was rinsed 3x with hexanes, pipetting the solvent out after each wash. The pellet was then

dried in an oven at 60 °C for 30 minutes. Between samples, the die was washed as above with hexanes preceding the water and ethanol.

2.2.8 Use of spacers in pellet formation in place of lubricant

Circular pieces of either aluminum foil or weigh paper were made using a hole punch and placed on the face of one or both anvil(s) prior to pressing. The spacers were separated from the pellet by soaking in ethanol for 5 minutes and gently lifting with tweezers.

2.2.9 Mixing of tungsten with calcium hydroxyapatite

Hydroxyapatite and tungsten containing compounds were mixed via one of three methods. **1)** The samples ground with a pestle and mortar were carefully weighed out on a balance followed by 10 – 15 minutes of continuous grinding before making the samples into pellets. **2)** Mixing in water with stirring, the samples were carefully weighed and put in a round bottom flask along with ~40 mL DI water and a stir bar, the flask was capped and left to stir overnight. In the morning the stirring was stopped, and the sample placed under vacuum to dry. **3)** Mixing in water via sonication, the samples were carefully weighed out and placed in a 50 mL falcon tube and was filled to the 40 mL mark. An ultra-sonication horn was inserted in the falcon tube about halfway down the tube, illustrated in **Scheme 2.** the opening of the falcon tube was wrapped in parafilm to avoid spills and the sample was sonicated for 30 minutes at 20 kHz. The sample was then dried under vacuum. Samples were made in concentrations of 5, 10, 20, 50, 100, 250 and 500 ppm of tungsten by mass. Sodium tungstate, calcium tungstate and phosphotungstate samples were all made for a total of 27 samples.

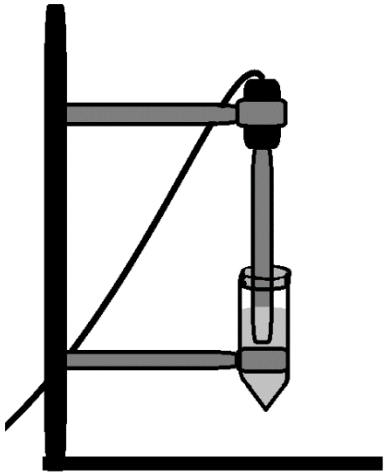

Scheme 2. Ultra-sonication horn setup.

2.2.10 Synthesis of hydroxyapatite

To a 500 mL 3-neck flask, 100 mL DI water were added. The 3-neck flask was outfitted with two addition funnels (100 mL and 20 mL) and a septum. N_2 was bubbled into the water and heated to 40 °C with stirring for one hour. The reaction was kept under N_2 until completion. To the water 3.71 g $Ca(OH)_2$ (50 mmol) were added. To the 100 mL addition funnel, 3.41 g 85% H_3PO_4 (30 mmol) in 100 mL water were added. To the 20 mL addition funnel 5.6 mL 30% NH_4OH in 20 mL water were added. The septum was removed, and a pH probe inserted into the flask. The neck was sealed with parafilm. Dropwise, the H_3PO_4 was added to the $Ca(OH)_2$ slurry, adding NH_4OH to maintain a pH ≥10. The pH probe was removed, and the septum replaced. The mixture was left to stir for three hours at 40 °C at which point the heat was turned off and the mixture was left to stir, under nitrogen, overnight. The next day, the sample was divided evenly into 50 mL falcon tubes and centrifuged down. The supernatant was removed, and DI water was added to the falcon tubes to the 50 mL mark. The samples were shaken and briefly sonicated to loosen the pellet, before being centrifuged down again. This process was repeated for another three cycles or until the pH

of the supernatant was neutral. The samples were left in the falcon tube with their caps loosened in an oven at 60 °C overnight to dry.

In the synthesis of tungsten-doped hydroxyapatite, 2 mL $NaWO_4 \cdot 2H_2O$ [14 mM] were added to the H_3PO_4, solution shortly before addition of the acid to the three-neck flask to obtain a theoretical tungsten concentration of 1000 ppm or 0.1 wt %. The volume of $NaWO_4 \cdot 2H_2$ was adjusted to meet the desired concentration.

2.2.11 Laser ICP-MS of tungsten-hydroxyapatite mixtures and tungsten-doped-hydroxyapatite

A selection of samples from **2.2.9** – **10** were measured for homogeneity using laser ICP-MS. Pellets of hydroxyapatite – sodium tungstate mixtures at 5, 50, and 500 ppm from all three of the mixing methods described in **2.2.9** were used, in addition to a 0.1 wt% (1000 ppm) sample of tungsten-doped hydroxyapatite and powdered calcium hydroxyapatite from Sigma-Aldrich as a control. Experiments were run with a spot size of 95 µm, repetition rate of 20 Hz, and a fluence of ~6 Jcm^{-2} (5.80-6.15). Scans were 300 µm per line, run at a speed of 5 μms^{-1} with a washout time of 40 seconds and five lines per sample.

2.2.12 Osteoclast seeding on tungsten-doped hydroxyapatite

Eleven samples were provided to be seeded with osteoclasts. Two of each; 500 ppm sodium tungstate – hydroxyapatite, 500 ppm calcium tungstate – hydroxyapatite, and 500 ppm tungsten-doped hydroxyapatite in addition to five tungsten-free hydroxyapatite pellets, one as a control to

not be seeded, two to be seeded with no tungsten present, and two to be seeded where the media is spiked with a small amount of aqueous tungsten.

Bone marrow was flushed from the femur, tibia, and humeri of C57BL/6, 8 – 10-week-old, male mice. Bone marrow was cultured in alpha-MEM (Wisent #310-010-CL), 10% FBS (Wisent #090150, lot#112660), and 1% penicillin/streptomycin (Wisent #450-201-EL) in a T75 flask with 25 ng/mL of macrophage colony stimulating factor (M-CSF, Peprotech#300-25) in order to enrich the myeloid population for pre-osteoclasts. The next day, the myeloid enriched pre-osteoclasts were seeded at 250,000 cells/well in a 24-well plate in 500 uL of complete growth media with 50 ng/mL of M-CSF on top of the hydroxyapatite-pellets. RANKL was added the following day after seeding at 50 ng/mL (Peprotech #315-11), in addition to 15 ppm tungsten if needed. Media was replenished every 2 days. Osteoclasts were cultured in RANKL for a total of 4 days. Unsure how TRAP staining would affect planned synchrotron measurements, the majority of samples were not TRAP stained, with the exception of the 500 ppm tungsten-doped hydroxyapatite. All samples were desiccated one week after seeding.

2.2.13 Canadian Light Source SR-μXRF spectra acquisition of osteoclast-seeded-tungsten-containing-pellets

Samples selected from those described in **2.2.12** were mounted on a motorized stage at 45° angle relative to the incident X-ray beam. A Single Element XMap Vortex Detector was used to collect the XRF spectra, which was placed in the horizontal polarization plane at 90^{o} to the incident X-ray beam (and 45^{o} to the sample) with a sample-to-detector distance of 40 mm. The SR-μXRF maps were generated from deadtime-corrected XRF spectra with normalization to the flux of

incident X-ray beam measured by an ion chamber. The pellets were surveyed using a light microscope. Features that roughly fit the size of a mature osteoclasts were selected for scanning, in addition to controls where the pellet(s) appeared flat and uniform.

2.2.14 Advanced Photon Source 2D XRF and XANES spectra acquisition of osteoclast-seeded-tungsten-containing-pellets

Samples selected from those described in **2.2.12-13** were chosen to acquire a higher resolution 2D XRF map than acquired in **2.2.13** in addition to identification of tungsten speciation via the XANES spectra. A beam size of is 5 µm x 5 µm was used. The monochromator was reported to be 10.8565 degrees, with an energy from motor reported at 10500.007 eV, and the KB and IDC slits were set to 140 mm wide x 210 mm high and 5 µm wide x 5 µm high, respectively. Due to travel restrictions we were unable to attend in person to select the areas of study for the scans. As a result, a shotgun approach was used.

2.3 Results & discussion

2.3.1 Preparation of biomimetic bone mimic pellets

We were able to reliably produce calcium hydroxyapatite (HAp) pellets with a diameter of 7 mm and a thickness of ~0.5 mm with improved success rate. Pressures of about 25 tons were used; higher pressures resulted in cracking of the pellet and increased the likelihood the pellet would stick to the anvil. Lower pressures resulted in lower density such that when submerged in solution over several days for subsequent cell experiments, the pellet would crumble.

Use of Kapton tape tabs on the backside of pellets reduced direct handling, which in turn reduced the frequency of cracking and chipping. The Kapton tape tabs can also serve as a reference point when mapping the pellets features.

2.3.2 Incorporation of collagen into a hydroxyapatite pellet

Use of 70:30 hydroxyapatite/collagen not only made the pellets more biomimetic, but also made the pellets more robust and easier to handle, exactly as collagen adds and tensile strength to bone, or steel bars in concrete. This is a known phenomenon, and organic binders such as wax or ethylene glycol are often used in pellets to increase the robustness or "green strength" during general handling.[17, 18] Ratios that deviate from the average 70:30 found in bone are considered in bone graft experiments concerned with implantation and incorporation, the above ratio was used in our experiments to most closely mimic the ratio found in bone.[19] Due to interference in fluorescence measurements of subsequent experiments, discussed in **3.4.4**, fluorescence imaging of hydroxyapatite pellets, collagen was omitted from the majority of pellets produced.

2.3.3 Use of lubricant in pellet formation

In trials lacking any ethanol, oil or spacers, the pellet and die would often stick to one another. Lubricants are known to reduce powder-die and powder-powder friction, making the pellet easier to eject and remove from the die as well as allowing the powder granules to more easily move past each other during compaction resulting in a better ordered and more compact pellet.[17] Use of pure Nujol oil almost completely eliminated the occurrence of the pellet sticking to one or both anvils. However, it is likely that during compaction of the pellet a small amount of lubricant is trapped

under the surface meaning a surface cleaning of hexanes would be insufficient as in subsequent experiments osteoclasts are expected to resorb the top layer of the pellet, potentially releasing the lubricant into the cell media. Therefore use of volatile lubricant that is easily removed with moderate to high heat, and why ethanol was chosen as the preferred lubricant.[18]

2.3.4 Use of spacers in pellet formation in place of lubricant

Use of spacers such as aluminum foil or weigh paper prevented fusion of the sample to the anvil but would often result in the spacer jammed onto the surface of the pellet. While this is not ideal, it could prove useful to use a spacer on one side of the sample if one anvil is particularly prone to sticking to the sample. Additionally, if the spacer were to be left on one side of the pellet it could distinguishing which side of the pellet is to be studied during and after seeding of cells in the event a pellet gets flipped via transport or general handling.

2.3.5 Mixing of tungsten with calcium hydroxyapatite

In order to study the influence of tungsten on osteoclast activity, it is important to have samples that have a uniform dispersion of tungsten. To do this we used laser ICP-MS to examine the relative amount of tungsten in a scan across a pellet. The aim was to achieve a tungsten distribution such that no matter where an osteoclast was seeded, the cell would always be over part of the pellet that contained tungsten. Given that osteoclasts grow to about 150 – 200 μm in diameter, measurements were performed with a 95 μm spot size where a consistent tungsten count would imply that any seeded osteoclast would likely be in contact with a tungsten molecule. Results are summarized in **Table 2.**

Table 2. Average ratio of $^{182}W/^{43}Ca$ counts measured using laser ICP-MS in tungsten-containing hydroxyapatite. Stock refers to powered hydroxyapatite acquired from Sigma-Aldritch. Ground, Stirred and Sonication refer to the samples prepared in section **2.2.9** using sodium tungstate dihydrate. Precipitation is synthesized tungsten-doped hydroxyapatite prepared as described in **2.2.10**.

Preparation method	0 ppm Average ± SD	5 ppm Average ± SD	50 ppm Average ± SD	500 ppm Average ± SD	1000 ppm Average ± SD
Stock	0.0				
Ground		$6.8\cdot10^{-3} \pm 2.8\cdot10^{-2}$	$9.1\cdot10^{-2} \pm 4.7\cdot10^{-1}$	$2.8\cdot10^{-1} \pm 3.8\cdot10^{-1}$	
Stirred		$5.7\cdot10^{-3} \pm 1.9\cdot10^{-2}$	$5.7\cdot10^{-2} \pm 1.8\cdot10^{-1}$	$1.4\cdot10^{-1} \pm 1.5\cdot10^{-1}$	
Sonication		$1.9\cdot10^{-3} \pm 2.5\cdot10^{-2}$	$2.7\cdot10^{-2} \pm 8.0\cdot10^{-2}$	$2.0\cdot10^{-1} \pm 2.3\cdot10^{-1}$	
Precipitation					$3.1\cdot10^{-1} \pm 3.4\cdot10^{-2}$

The resulting ICP-MS measurements show, on a scale of a 95 µm spot, that tungsten was not uniformly dispersed in the 5, 50 and 500 ppm samples with any of the mixing methods. At the time of these measurements, only 1000 ppm tungsten-doped hydroxyapatite was prepared to be measured. Subtracting the control as background, scans showed in each case a low W:Ca baseline with frequent spikes and a standard deviation larger than the average. The standard deviation is included here as an indication of homogeneity where a large SD relative to the mean indicates frequent areas of low and high counts and a low SD indicates a homogeneous dispersion.

In 5, 50, 500 ppm samples the standard deviation is greater than the mean where the difference is greatest at 5 ppm *i.e.* $6.8\cdot10^{-3} \pm 2.8\cdot10^{-2}$ and lowest at 500 ppm *i.e.* $2.0\cdot10^{-1} \pm 2.3\cdot10^{-1}$. The only preparation method to have a SD lower than the mean count was the synthesis via precipitation of hydroxyapatite in the presence of tungsten $3.1\cdot10^{-1} \pm 3.4\cdot10^{-2}$.

From these measurements, there are two explanations for the low standard deviation relative to the mean. The first is at some point between 500 – 1000 ppm tungsten, on the scale of 95 µm, dispersion using any of the above mixing methods would appear homogenous. The second is, when precipitated, tungsten is more uniformly distributed than other mixing methods. While we believe both explanations have merit, we proceeded assuming the latter was the primary cause. It should be noted that the value of 1000 ppm in the tungsten-doped hydroxyapatite is a theoretical value, assuming 100% yield and was not confirmed. An experiment to quantitively determine the loading efficiency of tungsten into hydroxyapatite by correlating tungsten signal from XPS of controls of known tungsten content to reference signal and comparing the values to tungsten doped hydroxyapatite. The full experiment is outlined in future work **4.2.1**.

Our suspicion was later confirmed by the 2D XRF maps generated at The Advanced Photon Source. While our aim was to generate images around osteoclasts and their pits, the shotgun approach failed to yield images of areas containing osteoclasts or resorption pits. However, we were able to visually compare the distribution of tungsten in the samples. **Figure 2** illustrates at 500 ppm calcium tungstate physically mixed with hydroxyapatite results in a dispersion of tungsten with a low background, but intense peaks, compared to 500 ppm tungsten-doped hydroxyapatite, which has more consistent values and lacks the extremes and is an indication of how uniformly the tungsten is distributed. It should be noted there is the possibility the synthesis of tungsten-doped hydroxyapatite did not incorporate 100% of the tungsten due to poor loading efficiency, resulting in a lower concentration of tungsten in the sample and could account for why the highs in **Figure 2D** are lower than **Figure 2B**. However, given that **Figure 2D** does not have the lows of **Figure 2B** indicated uniform dispersion.

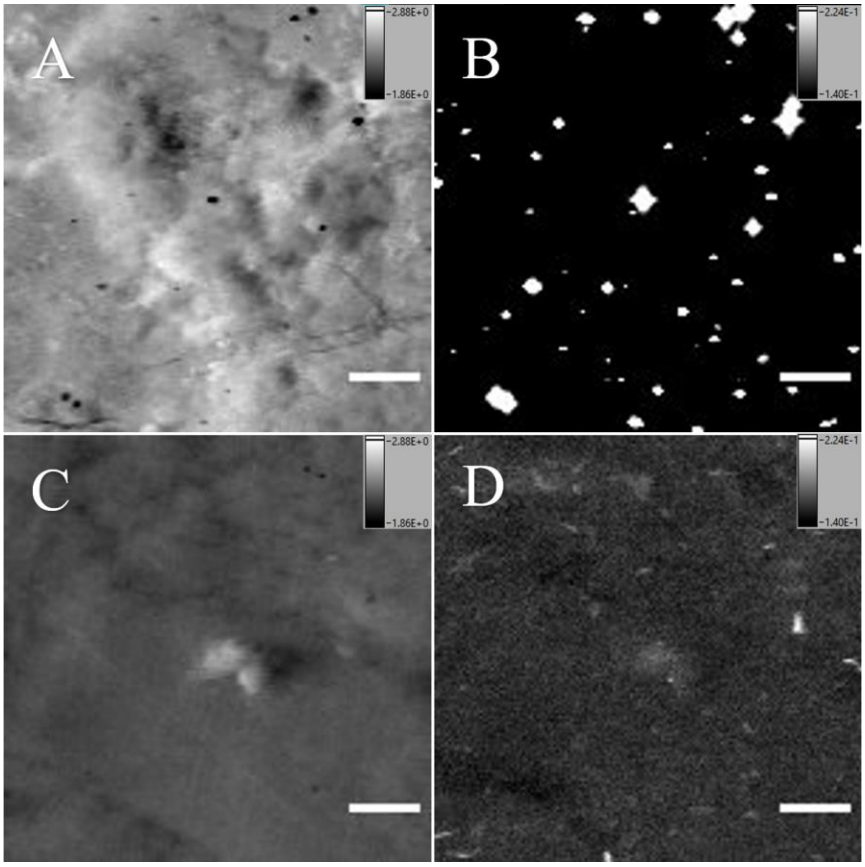

Figure 2. 2D XRF of (**A,B**) a 500 ppm mixture by tungsten weight of calcium tungstate and hydroxyapatite mixed via sounding horn and (**C,D**) 500 ppm by tungsten weight of tungsten-doped hydroxyapatite synthesized via precipitation. All images are referenced to I0, (**A,C**) plot CaKα and (**B,D**) plot WLα. Scale bars are 25 μm.

2.3.6 Canadian Light Source 2D XRF spectra acquisition of osteoclast-seeded-tungsten-containing-pellets

Samples were seeded with osteoclasts for one week before desiccation to preserve the cells. Scanned areas were selected using a light microscope selecting features assumed to be either osteoclasts or resorption pits based on size. Fewer than expected osteoclasts were found on pellets, possibly due to the cells being inadvertently scraped off during handling and transport following desiccation. It was also difficult to find and identify osteoclasts as only one pellet underwent the process of TRAP staining to visualize osteoclasts, which made finding clear cells on a colourless

pellet a challenge. This was done to prevent any interference in the measurements from the TRAP stain. As time was limited only a few pellets were selected for measurement, favoring the samples with the fewest variables, thus excluding our TRAP stained sample.

A recurring feature on samples seeded with osteoclasts is an area of low intensity immediately next to an area of high intensity, **Figure 3**. To ensure the feature was not an artifact of sample – beam orientation, the sample was rotated by 90° where the feature persisted.

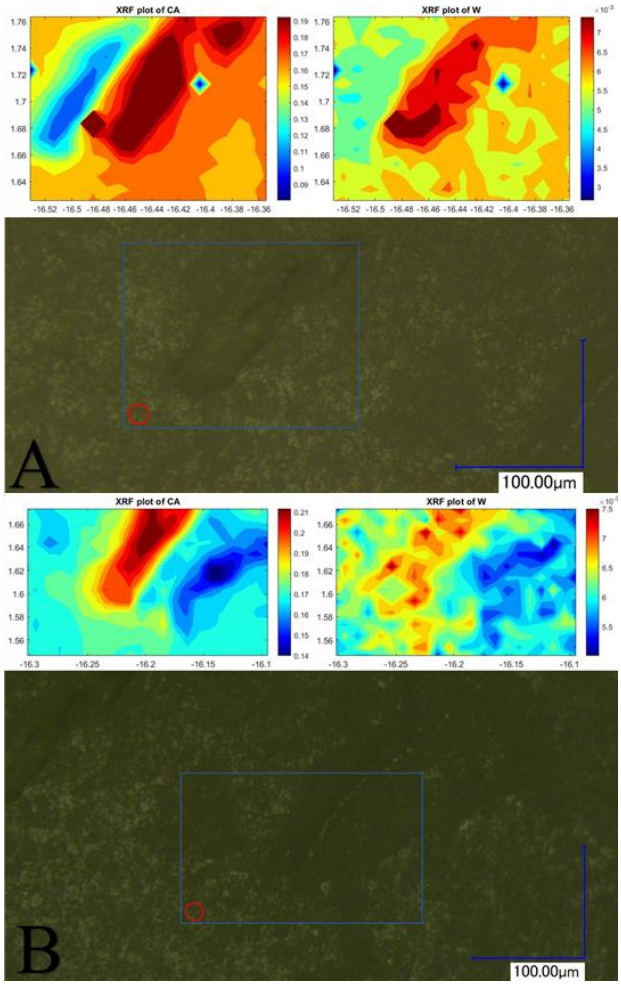

Figure 3. 2D XRF map of 500 ppm sodium tungstate – hydroxyapatite pellet seeded with osteoclasts. The blue box indicates the scanned area and corresponds to the intensity maps above. Scans were taken approximately 200 µm apart.

Areas of high intensity in one element with low intensity in another would suggest heterogenous distribution, such as in **Figure 2A&B**. Areas of high or low intensity for multiple elements suggests the beam passed through a higher or lower amount of material, *i.e.* the sample is not uniformly dense, or the surface is uneven. We propose in the above image, areas of low intensity are areas where an osteoclast had been resorbing material and the areas of high intensity are the osteoclasts themselves. It is possible that when the osteoclasts were desiccated, any material in the cell that had been recently resorbed and was in process of being released, was trapped in the cell, resulting in the areas of high intensity observed. Scanning electron microscopy images of osteoclasts by Monchau *et al.*, 2002 note most osteoclasts imaged were detached on one side, exposing the resorption pit.[20]

It is important to note that the features in **Figure 3A&B** were found on the same sample ~ 200 µm apart and the features mirror one another, with the areas of high intensity being closest to one another. This feature may be coincidence but may show that the cells were in the process of coming together to fuse into a larger, mature osteoclast.[21, 22]

2.3.7 Advanced Photon Source XANES spectra of osteoclast-seeded-tungsten-containing-pellets

XANES spectra were obtained with the aim to determine the species of tungsten in the tungsten-doped hydroxyapatite and determine if osteoclast activity results in alteration of tungsten speciation. The change in XANES spectra between tungsten species is subtle, shown in **Figure 4A1-C1**, and as such it is easier to visualize using the second derivative, shown in in **Figure 4A2-C2**.

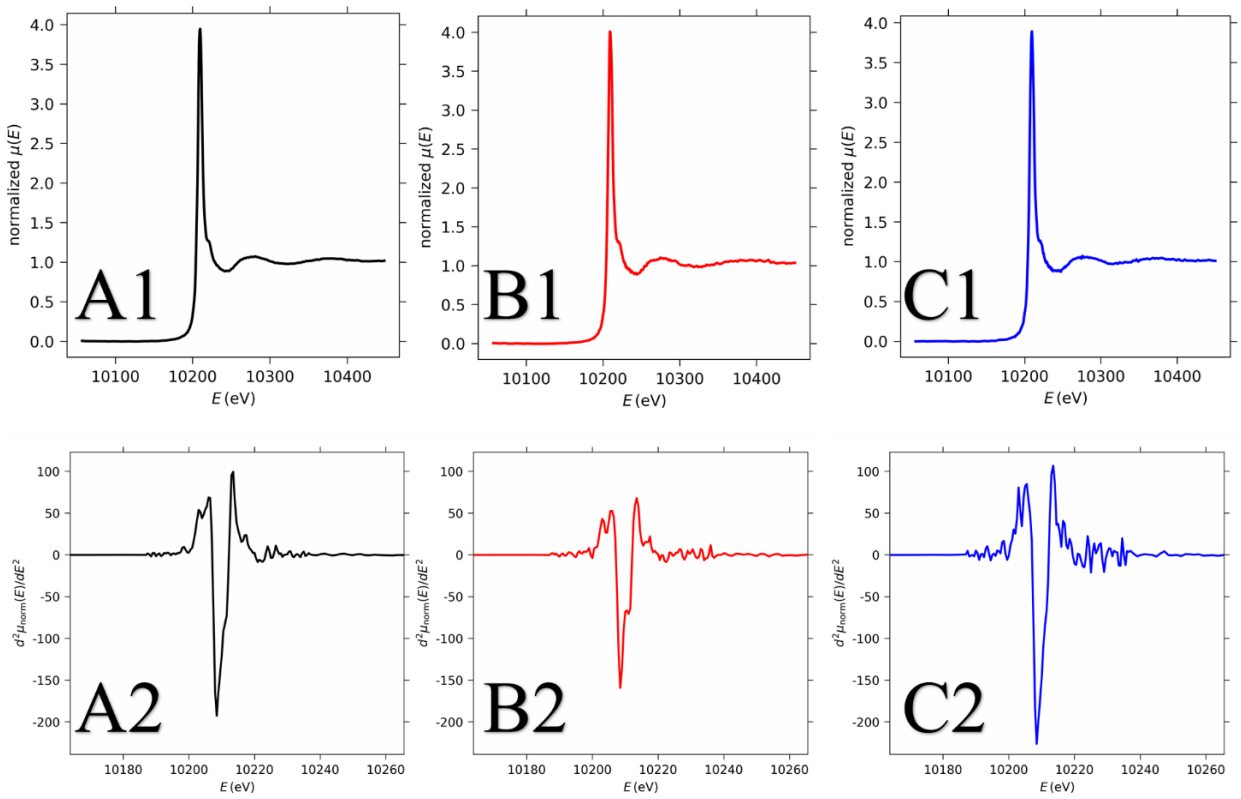

Figure 4. XANES spectra for tungsten in tungsten-doped hydroxyapatite pellet seeded with osteoclasts. **A)** Average of all scans **B,C)** Single scan examples **Row 1)** Normalized µE **Row 2)** Second derivative of µE.

Comparing the scans to previous studies in our group, shown in VanderShee *et al*, 2018, our spectrum in **Figure 4C2** most closely resembles the control for sodium tungstate.[23] The strong single peak is consistent with the tetrahedral coordination observed in monotungstates.[23, 24] We believe the acidic microenvironment during osteoclast resorption facilitates the alteration of tungsten speciation. Due to travel restrictions we were unable to attend in person to select and acquire light microscope images of the scanned areas. If this model holds, then **Figure 4C2** was scanned in an area with no osteoclast activity and represents background tungsten. The secondary peak in **Figure 4B2** suggests a small amount of an alternate tungsten species and is converging

towards a spectrum similar to the tungsten species found in bone, which has previously been shown to be most similar to phosphotungstate.[23] The formation of a second peak is consistent with a distorted octahedral of seen in many polytungstates.[23, 24] For the model to be true, **Figure 4B2** was taken either on an osteoclast, or pit where an osteoclast had been resorbing. During resorption, the acidic microenvironment of the osteoclast dissolves the components of bone. It is possible that tungsten enters the microenvironment, either already existing in solution or liberated during resorption, and reacts with the calcium and phosphate ions of hydroxyapatite, precipitating out of solution as polytungstates, accumulating in the sample, or in some cases, bone. As the pellet is 500 ppm tungsten by mass, during the one week which the osteoclasts were seeded only a relatively small amount would be resorbed and converted, leaving the majority of tungsten in the sample unaffected. This would explain why in **Figure 4B2** the primary peak correlates most closely to sodium tungstate and why the secondary peak in **Figure 4A2**, the average over six scans, is so small.

2.4 Conclusion

We have devised a procedure to increase the success rate of hydroxyapatite pellet formation. We incorporated collagen thereby increasing green strength while making the sample more biomimetic. To the pellets, several species of tungsten was incorporated via variety of mixing methods. Using laser ICP-MS and 2D XRF we have determined precipitation of hydroxyapatite in the presence of tungsten results in the most uniform dispersion. 2D XRF maps of osteoclasts and resorption pits have been acquired. Tungsten XANES spectra suggest osteoclasts could be responsible for conversion of tungsten species *in vitro*.

2.5 References

1. Florencio-Silva, R.; Sasso, G. R. d. S.; Sasso-Cerri, E.; Simões, M. J.; Cerri, P. S., Biology of Bone Tissue: Structure, Function, and Factors That Influence Bone Cells. *BioMed Research International* **2015,** *2015*, 421746.
2. Sieberath, A.; Della Bella, E.; Ferreira, A. M.; Gentile, P.; Eglin, D.; Dalgarno, K., A Comparison of Osteoblast and Osteoclast In Vitro Co-Culture Models and Their Translation for Preclinical Drug Testing Applications. *Int. J. Mol. Sci.* **2020,** *21*, 912.
3. Rao, H.; Tan, J.; Faruqi, F.; Beltzer, J., Corning® Osteo Assay Surface: A New Tool to Study Osteoclast and Osteoblast Differentiation and Function. Corning Incorporated Sullivan Park, NY 14831: 2011.
4. Manninen, O.; Puolakkainen, T.; Lehto, J.; Harittu, E.; Kallonen, A.; Peura, M.; Laitala-Leinonen, T.; Kopra, O.; Kiviranta, R.; Lehesjoki, A.-E., Impaired osteoclast homeostasis in the cystatin B-deficient mouse model of progressive myoclonus epilepsy. *Bone Reports* **2015,** *3*, 76-82.
5. ARNETT, T. R.; DEMPSTER, D. W., Effect of pH on Bone Resorption by Rat Osteoclasts in Vitro. *Endocrinology* **1986,** *119* (1), 119-124.
6. Mehta, M.; Schmidt-Bleek, K.; Duda, G. N.; Mooney, D. J., Biomaterial delivery of morphogens to mimic the natural healing cascade in bone. *Advanced Drug Delivery Reviews* **2012,** *64* (12), 1257-1276.
7. Zhao, B.; Hu, H.; Mandal, S. K.; Haddon, R. C., A Bone Mimic Based on the Self-Assembly of Hydroxyapatite on Chemically Functionalized Single-Walled Carbon Nanotubes. *Chemistry of Materials* **2005,** *17* (12), 3235-3241.
8. Venkatesan, J.; Bhatnagar, I.; Manivasagan, P.; Kang, K.-H.; Kim, S.-K., Alginate composites for bone tissue engineering: A review. *International Journal of Biological Macromolecules* **2015,** *72*, 269-281.
9. Schilling, A. F.; Linhart, W.; Filke, S.; Gebauer, M.; Schinke, T.; Rueger, J. M.; Amling, M., Resorbability of bone substitute biomaterials by human osteoclasts. *Biomaterials* **2004,** *25* (18), 3963-3972.
10. Gu, F.; Amsden, B.; Neufeld, R., Sustained delivery of vascular endothelial growth factor with alginate beads. *Journal of Controlled Release* **2004,** *96* (3), 463-472.
11. Koutsospyros, A.; Braida, W.; Christodoulatos, C.; Dermatas, D.; Strigul, N., A review of tungsten: From environmental obscurity to scrutiny. *Journal of Hazardous Materials* **2006,** *136* (1), 1-19.
12. Bednar, A. J.; Jones, W. T.; Boyd, R. E.; Ringelberg, D. B.; Larson, S. L., Geochemical Parameters Influencing Tungsten Mobility in Soils. *Journal of Environmental Quality* **2008,** *37* (1), 229-233.
13. Rubin, C. S.; Holmes, A. K.; Belson, M. G.; Jones, R. L.; Flanders, W. D.; Kieszak, S. M.; Osterloh, J.; Luber, G. E.; Blount, B. C.; Barr, D. B.; Steinberg, K. K.; Satten, G. A.; McGeehin, M. A.; Todd, R. L., Investigating Childhood Leukemia in Churchill County, Nevada. *Environmental Health Perspectives* **2007,** *115* (1), 151-157.
14. Seiler, R. L.; Stollenwerk, K. G.; Garbarino, J. R., Factors controlling tungsten concentrations in ground water, Carson Desert, Nevada. *Applied Geochemistry* **2005,** *20* (2), 423-441.
15. Guandalini, G. S.; Zhang, L.; Fornero, E.; Centeno, J. A.; Mokashi, V. P.; Ortiz, P. A.; Stockelman, M. D.; Osterburg, A. R.; Chapman, G. G., Tissue Distribution of Tungsten in Mice

Following Oral Exposure to Sodium Tungstate. *Chemical Research in Toxicology* **2011,** *24* (4), 488-493.
16. Gong, J. K.; Arnold, J. S.; Cohn, S. H., Composition of trabecular and cortical bone. *The Anatomical Record* **1964,** *149* (3), 325-331.
17. Lemoisson, F.; Froyen, L., Understanding and improving powder metallurgical processes. **2005**, 474-502.
18. Mizzan, E.; Chalder, G. H. *Comparison of binder/lubricant additives in dry pressing uranium dioxide powder*; AECL-660; CRFD-757 Canada DTIE English; ; Atomic Energy of Canada Ltd., Chalk River, Ontario (Canada). Chalk River Project: 1958; p Medium: ED; Size: Pages: 18.
19. Wang, J.; Liu, C., Biomimetic Collagen/Hydroxyapatite Composite Scaffolds: Fabrication and Characterizations. *Journal of Bionic Engineering* **2014,** *11* (4), 600-609.
20. Monchau, F.; Lefèvre, A.; Descamps, M.; Belquin-myrdycz, A.; Laffargue, P.; Hildebrand, H. F., In vitro studies of human and rat osteoclast activity on hydroxyapatite, β-tricalcium phosphate, calcium carbonate. *Biomolecular Engineering* **2002,** *19* (2), 143-152.
21. Jansen, I. D. C.; Vermeer, J. A. F.; Bloemen, V.; Stap, J.; Everts, V., Osteoclast Fusion and Fission. *Calcified Tissue International* **2012,** *90* (6), 515-522.
22. Hobolt-Pedersen, A.-S.; Delaissé, J.-M.; Søe, K., Osteoclast Fusion is Based on Heterogeneity Between Fusion Partners. *Calcified Tissue International* **2014,** *95* (1), 73-82.
23. VanderSchee, C. R.; Kuter, D.; Bolt, A. M.; Lo, F.-C.; Feng, R.; Thieme, J.; Chen-Wiegart, Y.-c. K.; Williams, G.; Mann, K. K.; Bohle, D. S., Accumulation of persistent tungsten in bone as in situ generated polytungstate. *Communications Chemistry* **2018,** *1* (1), 8.
24. Hur, H.; Reeder, R. J., Tungstate sorption mechanisms on boehmite: Systematic uptake studies and X-ray absorption spectroscopy analysis. *Journal of Colloid and Interface Science* **2016,** *461*, 249-260.

Chapter 3

Fluorescence Study of Biomimetic Hydroxyapatite Pellets

3.1 Introduction

In the previous chapter we established 2D XRF and XANES X-ray techniques have been used to study osteoclasts and their interaction with tungsten doped hydroxyapatite. Those X-ray techniques, while not widely accessible, were used with the aim to determine tungsten speciation. This chapter will develop a fluorescent probe to follow osteoclast function in the presence of tungsten.

Osteoclast visualization typically involves staining of tartrate-resistant acid phosphatase (TRAP), an enzyme that is associated with proper osteoclast function and is observed in single nuclei juveniles as well as the ruffled boarder of mature osteoclasts, making differentiation between mature and newly fused cells relatively straightforward.[1-3] One disadvantage of TRAP staining is that it results in the death of the osteoclast, so while it has been invaluable for the identification and study of the morphology of osteoclasts, TRAP staining is not suitable for the study of *in vivo*

cellular functions. Osteoclasts are believed to use cathepsin K to dissolve the collagen and other organic materials of bone, while acid dissolves the inorganic matrix.[4, 5] It was not until 2009 that cathepsin K in live osteoclasts was observed *in vivo*, and a procedure to visualize the changing pH *in vivo* developed in 2011.[5, 6] To detect the changing pH the Kikuchi group used pH sensitive boron-dipyrromethene (BODIPY) dyes, **Table 3**, which they dubbed BAp-M and pHocas-1.[5, 7] Bisphosphonate moieties were incorporated into the dyes to give an affinity for bone, and acid-sensitive aryl groups were selected to tune the pK_a of the dye to turn its fluorescence off under physiological pH and on during osteoclast resorption as a result of the acidification.

Our focus, as mentioned in Chapter 2, is the study of osteoclast function in the presence of tungsten. Under basic conditions monomeric tungstates are predominant and are soluble, and in general are considered non-toxic but as the pH decreases to acidic levels, monotungstates are able to polymerize to a variety of isopolytungstates and heteropolytungstates, of which the toxicity has not been well studied and has recently been called into question.[8-11] The use of a pH sensitive BODIPY could afford valuable insight into osteoclast activities when exposed to tungsten. At physiological pH, photoinduced electron transfer (PET) from the aryl substituent quenches the fluorophore, but at low pH when the amine group is protonated, the change in electronic structure ceases the quenching mechanism and results in strong emission.[12] Great care was taken to synthesize and fully characterize our dye, **BODIPY 1**. What was not anticipated was the overlapping of the excitation and emission curves of **BODIPY 1** with the main components of bone, hydroxyapatite and collagen. These complications pushed us to consider alternate avenues including sintering of hydroxyapatite to quench the inherent fluorescence and use of europium as a fluorescent indicator.

Table 3. BODIPY structures used to compare the photophysical properties of **BODIPY 1**.

Name/source	Structure
BODIPY 1	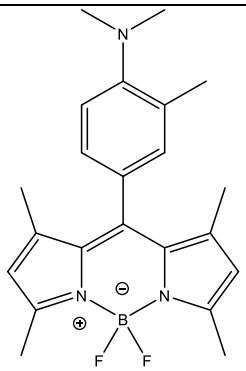
Fluorescent indicator 1 Werner *et al.*, 1997.[13]	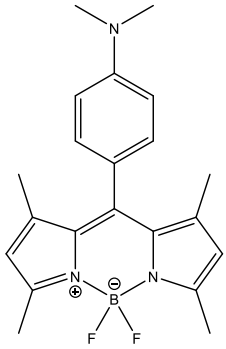
BAp-M Kowada *et al.*, 2011.[5] Kikuchi group	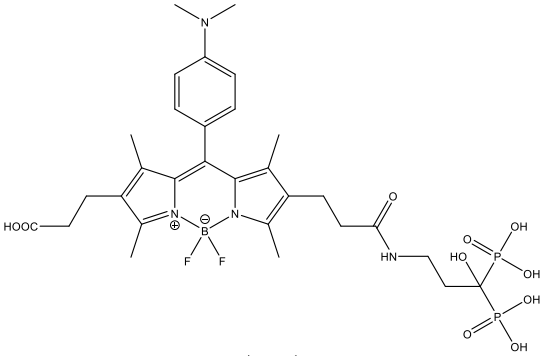
pHocas-1 Maeda *et al.*, 2016.[7] Kikuchi group	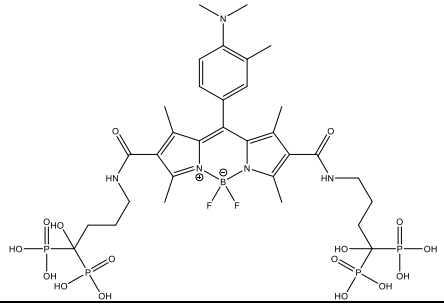

3.2 Materials and methods

3.2.1 NMR

^{1}H, ^{19}F, and ^{13}C NMR spectra were acquired on a Bruker AVIIIHD 500 MHz NMR Spectrometer.

3.2.2 UV-Vis

UV-Visible spectra were acquired from 300 - 700 nm using an HP Agilent 8453 diode array spectrophotometer.

3.2.3 Fluorimeter

Fluorescence spectroscopy was carried out using a Photon Technology International (PTI) Quanta Master fluorimeter and analyzed on FeliX32 version 1.2 software. 1 x 1 cm glass cuvettes were used for fluorescence measurements. Excitation and emission slits were set to 1.2 nm. Samples were excited at 470 nm.

3.2.4 Fluorescent imaging

Fluorescent images were obtained on a Zeiss AxioObserver Automated Inverted Microscope using a Hamamatsu 3900 x 3900 Monochrome camera and FS 24 (FITC) fluorescent cube. Deconvolution was performed using Zeiss ZEN 2 software suite. 2,2 binning was used.

3.2.5 Crystallography

Crystals were mounted on glass fibre with epoxy resin and single-crystal X-ray diffraction experiments are carried out with a BRUKER APEX-II CCD diffractometer by using graphite-monochromated MoKα radiation (λ = 0.71073 Å) SAINT[14] was used for integration of the intensity reflections and scaling and SADABS for absorption correction. Intrinsic phasing was used to solve the structures. Non-hydrogen atoms are located by difference Fourier maps and final solution refinements are solved by full-matrix least-squares method on F2 of all data, by using SHELXTL[15] software. The hydrogen atoms were placed in calculated positions.

3.2.6 Mass spectrometry

Electrospray ionization mass spectrometry was performed using an Exactive Plus Orbitrap-API from Thermo scientific.

3.2.7 Sintering

Samples were sintered in a Lindberg/Blue M Tube furnace Model STF55433C-1 in a platinum crucible at 1250 °C with a ramp of 10 °C per minute, followed by a dwell time of eight hours at which point the oven was cooled naturally at an approximate rate of 3 °C per minute.

3.2.8 Synthesis of pH sensitive BODIPY dye

The synthesis was based on the pH sensitive dye, pHocas-1, presented in Maeda *et al*, 2016, and following the procedure for synthesis of BODIPY dyes from Toja *et al.*, 1984 in Maeda *et al*, 2016, and Schoder *et al.*, 2017.[7, 16]

A mixture of *N*,*N*-dimethyl-*o*-toluidine (2.66 g, 19.9 mmol), hexamethylenetetramine (3.13 g, 22.3 mmol), acetic anhydride (2.42 g, 23.7 mmol) and paraformaldehyde (2.10 g, 70 mmol) in acetic acid (300 mL) was heated to reflux for 24 hours resulting in an amber solution. To the solution conc. H_2SO_4 (1.2 mL) was added and the solution then heated to reflux for one hour. The solution was cooled to room temperature. To the solution, 2 N *aq.* NaOH (2·100 mL) was added. The product was extracted with CH_2Cl_2 (3·100 mL). The organic layers were combined, washed with brine (100 mL) and dried over anhydrous $MgSO_4$ and concentrated under reduced pressure. The product, 4-(*N*,*N*-Dimethylamino)-3-methylbenzaldehyde, was carried forward without further purification.

In a 50 mL round bottom 0.155 g 4-(*N*,*N*-Dimethylamino)-3-methylbenzaldehyde (1.0 mmol) in 10 mL dichloromethane were added, followed by 0.181 g 2,4-dimethylpyrrole (1.9 mmol) in 10 mL dichloromethane. To the orange solution, two drops of trifluoracetic acid were added and left to stir for two hours, resulting in a red solution. Excess tetrachloro-1,4-benzoquinone was added and left to stir overnight, resulting in the BODIPY precursor shown above. The reaction mixture was washed with a sodium bicarbonate solution, followed by a brine wash and dried over $MgSO_4$. The solvent was removed under reduced pressure and the product was used without further purification as a BODIPY precursor in the following reaction.

To the BODIPY precursor dissolved in dichloromethane, 30 eq triethylamine in toluene were added and heated at 70° C for 30 min with stirring. To the mixture, 40 eq boron trifluoride diethyl etherate were added and refluxed for 2 hours. The reaction mixture was cooled to room temperature and the solvent removed under reduced pressure. The product was purified by column chromatography, using 30% dichloromethane in hexanes.

BODIPY 1. Yield over three reactions: 2%. Orange powder. ^{1}H, ^{13}C and ^{19}F NMR and ESI^{+} MS of the product are shown in **Supplemental Figures 1-4**. ^{1}H NMR ($CDCl_3$, 500.30 MHz): δ 7.08 (m, 1H), 7.03 (m, 1H), 7.00 (m, 1H), 2.75 (s, 6H), 2.55 (s, 6H), 2.34 (s, 3H), 1.43 (s, 6H). ^{13}C NMR ($CDCl_3$, 125.81 MHz): δ 155.1, 153.7, 143.3, 143.3, 142.7, 132.5, 131.9, 130.7, 128.5, 126.1, 121.1, 118.7, 44.3, 18.7, 14.7, 14.7. ^{19}F NMR ($CDCl_3$, 470.71 MHz): δ 146.35 (q, J = 32.9 Hz). HRMS ESI^{+} for $C_{22}H_{27}N_3BF_2$ (M+H) calcd: 382.2261, found: 382.2271.

3.2.9 Extinction coefficient determination

UV-Vis absorbance spectra were acquired using a 1 cm x 1 cm glass cuvette. The instrument was baselined using methanol. A stock solution of known concentration was titrated into the methanol and the absorbance spectrum was measured following each addition for a range of concentrations. The absorbance maxima (499 nm) were plotted against the concentrations to determine the extinction coefficient according to Beer's law.

3.2.10 UV-Vis pK_a determination

Using strong acid and strong base, aliquots of DI water were titrated in steps of approximately 0.5 pH units. A small amount of **BODIPY 1** was dissolved in methanol, resulting in a concentration of $3.22 \cdot 10^{-3}$ M. To a 1 cm x 1 cm glass cuvette, 1980 μL of acid/base solution were added and the UV-vis spectrum acquired and set as the baseline, after which 20 μL of dye were added and UV-vis spectrum acquired. The pH was remeasured and recorded. The procedure was repeated for all samples. The ratio of absorbance between 500 nm and 520 nm were plotted against pH. A Boltzmann fit was applied where the inflection point indicates the pK_a.

3.2.11 Fluorescence excitation and emission determination

Excitation and emission slits were on the fluorimeter set to 1.2 nm. Samples were measured in a 1 cm x 1 cm glass cuvette. The emission spectrum was collected from 480 nm to 750 nm, with excitation at 470 nm. The excitation spectrum was obtained by exciting with a range of wavelengths from 400 nm to 600 nm, measuring the emission at 510 nm. Emission and excitation spectra were obtained at pH 4.09 and pH 8.70.

3.2.12 Fluorescence pK_a determination

Using dilute HCl and NaOH solutions, solutions in DI water in steps of approximately 0.5 pH units were prepared. Slits on the fluorimeter were set to 1.2 nm. The fluorescence of each acid/base (1980 μL) solution was measured to be used as baseline. 20 μL of dye of concentration $8.92 \cdot 10^{-3}$ M were added for a total volume of 2 mL. The pH was remeasured after this addition and recorded.

The dye was excited on the shoulder at 470 nm. The integrated fluorescence spectra were plotted against pH. A Boltzmann fit was applied where the inflection point indicates the pK_a.

3.2.13 Addition of BODIPY dye to hydroxyapatite pellets

The dye was added to the pellet in one of three ways; **1)** suspension of hydroxyapatite powder in methanol, addition of a small amount of a solution of the dye in methanol, followed by removal of solvent by rotary evaporation. **2)** Soaking a preformed pellet in a methanol solution containing dye for 30 minutes, removing the pellet from the solution and allowing to dry before storing. **3)** To a preformed pellet, 2-3 drops of dye dissolved in methanol were added and left to evaporate.

3.2.14 Fluorescence imaging of hydroxyapatite pellets

Pellets were prepared as described in **2.2.5**. Dye was applied to the pellets as described in **3.2.13**. Fluorescent images were obtained using a FS 24 (FITC) fluorescent cube, exciting from 455-495 nm and capturing the emission between 505-555 nm. A magnification of 20x, depth of focus of 45 µm and 2,2 binning were used. Unless otherwise specified an exposure time of 25 ms was used. Exposure times were chosen based on the sample that was expected to show the highest fluorescence intensity, adjusting so the detector is not oversaturated. Only samples collected on the same day under the same exposure conditions are directly compared. Images are tiled together to give an overall view of the sample. Image intensity maxima was chosen based on the sample with the highest fluorescence intensity, similar to exposure time.

To a Corning 24-well plate, 2 mL citrate-phosphate [0.15 M] buffer of the desired pH were added, followed by the pellet to ensure the face of the pellet had come in contact with the buffer before imaging with the inverted microscope. The well plate was gently rocked until the pellet was submerged. All pellets were placed in the well plate before measurements were taken.

3.2.15 Sintering of hydroxyapatite

Hydroxyapatite powder was placed in a platinum crucible and placed in a sintering oven which was heated to 1250 °C with a ramp of 10 °C per minute, followed by a dwell time of eight hours at which point the oven was cooled naturally at an approximate rate of 3 °C per minute. Once cooled, the crucible was removed. The colourless hydroxyapatite reduced in volume by ~50 % and had a blue colour.

3.3 Results and discussion

3.3.1 BODIPY 1 synthesis and characterization

The aldehyde was synthesized via the Duff reaction of *N*,*N*-dimethyl-*o*-toluidine and acetic anhydride, using hexamethylenetetramine and paraformaldehyde.[16, 17] The dipyrrin was synthesized by acid-catalyzed condensation of the aldehyde and 2,4-dimethylpyrrole, followed by oxidation of the resulting dipyrromethane.[12] Triethylamine was used to deprotonate the dipyrrin to allow chelation of the boron, completing the BODIPY.[12] The reactions are outlined in **Scheme 3**.

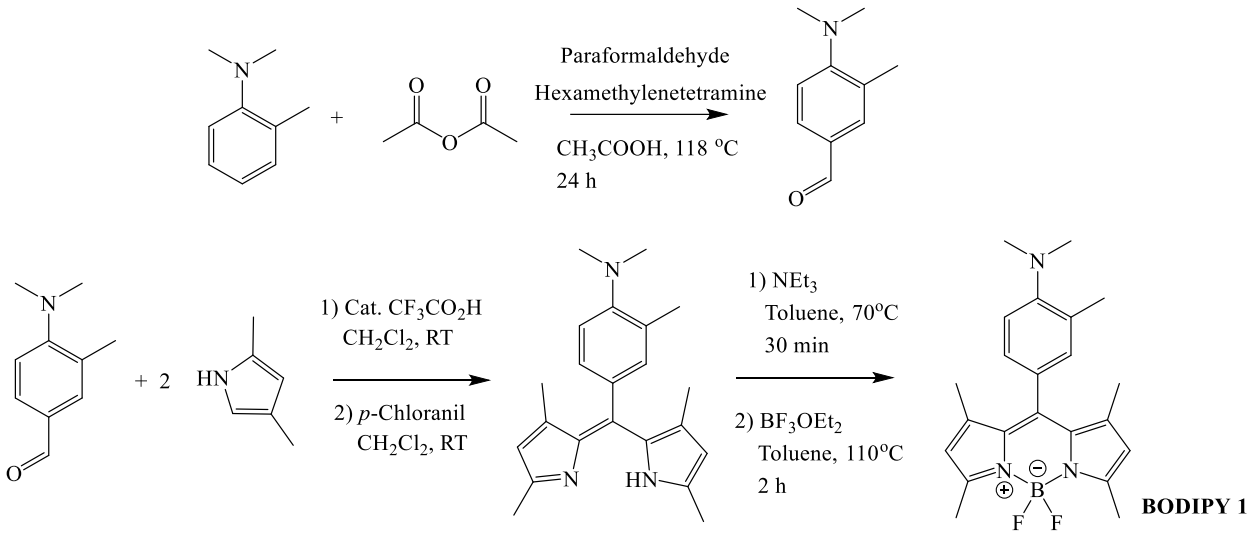

Scheme 3. Synthesis of **BODIPY 1.**

The identity of the product was confirmed by ^{1}H, ^{13}C, and ^{19}F NMR, mass spectrometry and single-crystal X-ray diffraction, **Supplemental Figure 1-5**. The splitting of ^{19}F NMR by ^{11}B, spin 3/2, results in a 1:1:1:1 quartet indicating that the two fluorine atoms have the same environment and they either do not interact with the methyl on the aryl group, or the aryl group spins rapidly on the NMR timescale. We know from number of unique ^{13}C peaks and ^{1}H NMR splitting pattern in the aromatic region that the phenyl ring is trisubstituted. These three observations indicate that they aryl group rotates rapidly. It would be interesting to perform ^{19}F NMR at lower temperatures to see if there are any changes to the fluorine splitting pattern.

The extinction coefficient (ε) was calculated using the Beer-Lambert law to be approximately 14,000 $M^{-1}cm^{-1}$ shown in **Supplemental Figure 6**. The UV-vis maxima was found at 499 nm, shown in **Figure 5**. The fluorescence emission spectrum was found at 510 nm, shown in **Figure 6**.

3.3.2 pK_a determination of BODIPY 1

As we did not plan to use our dye *in vivo* the amide – bisphosphonate side chains found in BAp-M and pHocas-1 responsible for binding to bone were omitted. This reduces the number of synthetic steps required and resulting in a new dye with similar functionality.

To test the functionality of **BODIPY 1** we obtained the excitation and emission under acidic (pH 4.09) and basic (pH 8.70) conditions. We observed strong emission and excitation signals under acidic conditions, and little to no signal under basic, illustrated in **Figure 5**.

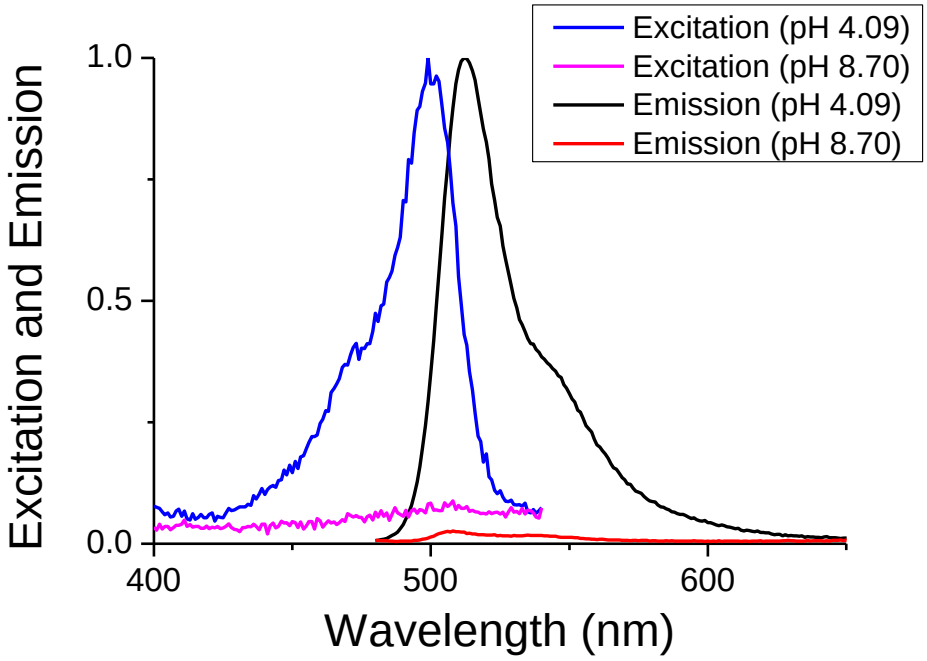

Figure 5. Fluorescence excitation and emission spectra of **BODIPY 1** under acidic and basic conditions. Excitation curves are normalized to the maximum excitation under acidic conditions. Emission curves are normalized to the maximum emission under acidic conditions.

Having demonstrated **BODIPY 1** was functional, we obtained absorbance and emission spectra over a range of pH levels to determine the pK_a and subsequently the range of pH values in which **BODIPY 1** would be useful. The absorbance spectra in **Figure 6** show a distinct curve change and ~5 nm red shift of the maxima under neutral and basic pH compared to acidic conditions.

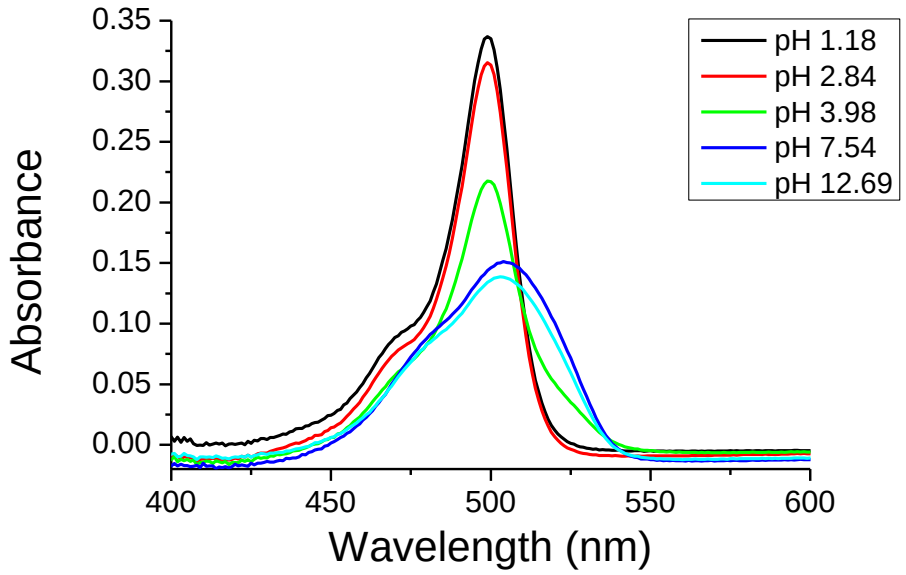

Figure 6. Selection of UV-vis spectra of **BODIPY 1** under a range of pH levels. A distinct change in curve shape is observed between pH 2.84 and pH 7.54, with a transition peak at pH 3.98.

Using the ratio of absorbance between 500 and 520 nm, we were able to illustrate a sigmoidal relationship between pH and state of protonation of **BODIPY 1**, shown in **Figure 7**. Using a Boltzmann fit the inflection point in the ground state is estimated to be pH 4.2.

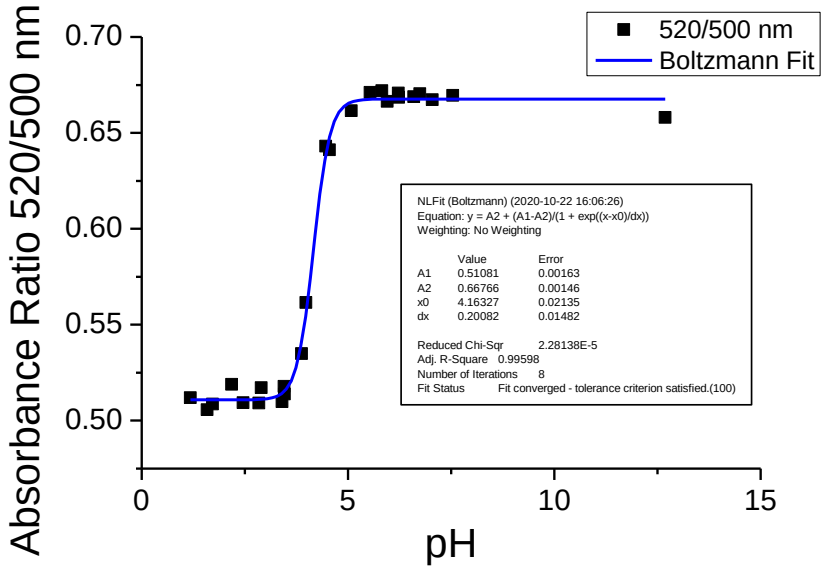

Figure 7. Ratio of UV-vis absorbance at two wavelengths across a range of pH levels. Inflection point at pH 4.2 illustrates the pK_a of **BODIPY 1** in the ground state.

During fluorescence measurements, it has been demonstrated that the increased energy of the excited state can alter the pK_a of molecules.[18] To determine the pK_a of **BODIPY 1** in the excited state we first measured the fluorescence intensity over a range of pH values, similar to our UV-vis study, shown in **Figure 8**. We then integrated the fluorescence intensity and plotted it against pH, generating a sigmoidal relationship, shown in **Figure 9**, we used a Boltzmann fit to determine the pK_a of 3.5.

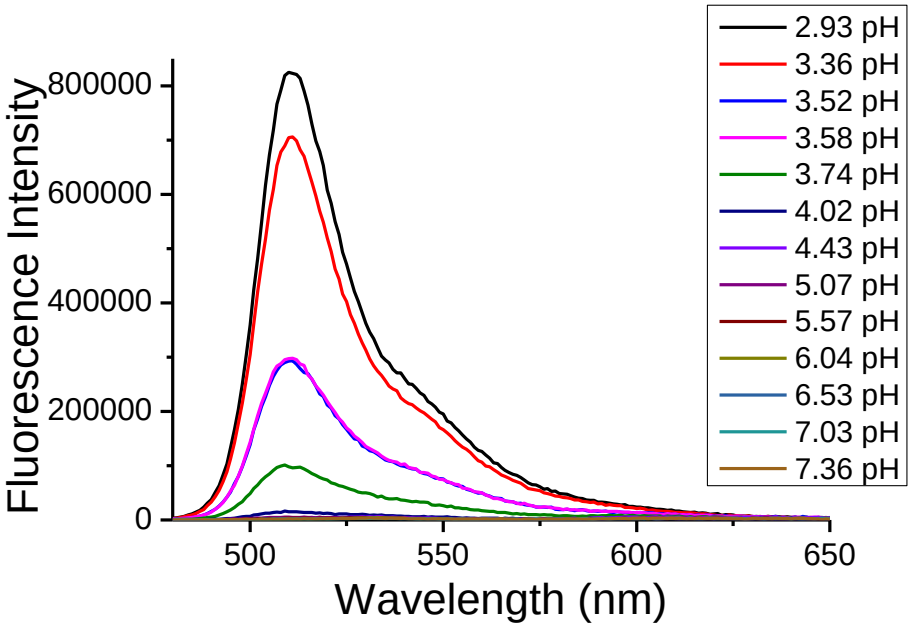

Figure 8. Fluorescence emission spectra of **BODIPY 1** excited at 470 nm across a range of pH.

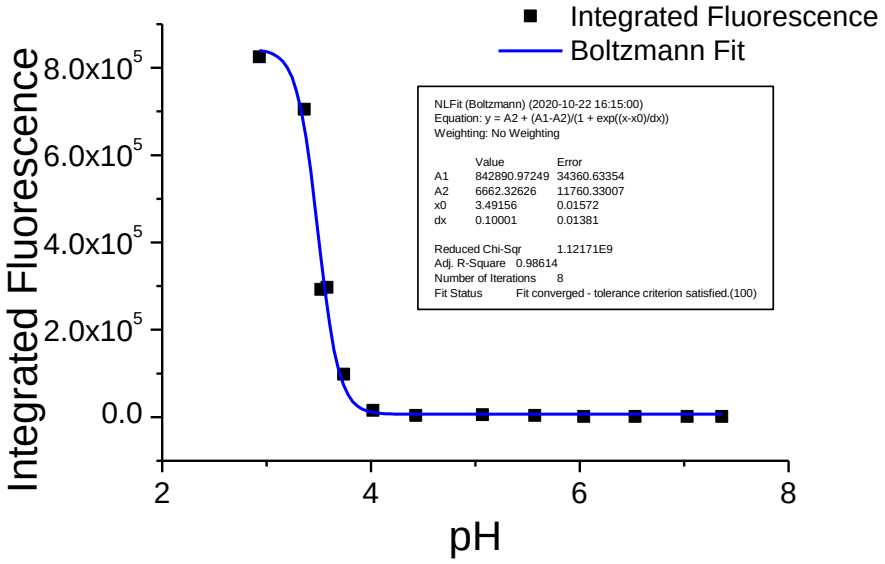

Figure 9. Integrated fluorescence at various pH. The inflection point of 3.5 illustrates the pK_a of **BODIPY 1** in the excited state.

We have determined the pK_a of **BODIPY 1** in the ground and excited state, pK_a = 4.2 and 3.5, respectively. In comparison, pHocas-1, the dye which **BODIPY 1** was based reported a pK_a of 5.3 determined from the fluorescence quantum yield.[7] Bap-M was determined to have a pK_a of 4.5 determined from the fluorescence quantum yield and Henderson-Hasselbach equation.[5] The change in pK_a from 5.3 of pHocas-1 to 4.5 Bap-M is likely due to the omission of the methyl group ortho to the amine.

Werner *et al*., 1997 report pK_a values for Fluorescent indicator 1, using fluorescence intensity and the Henderson-Hasselbach equation report two pK_a values; 3.30 and 2.31 in mixtures of 1:1 and 1:3 methonol:water, respectively.[12, 13] pK_a values of acids have been shown to increase with increasing methanol:water proportions, and makes direct comparison of 'Fluorescent indicator 1' and **BODIPY 1** unreliable as our measurements used a ratio of 1:99 methanol:water.[18, 19] Using the same comparison of pHocas-1 to Bap-M, it appears the additional methyl group on **BODIPY 1** is responsible for a change of pK_a ~1 comparing of fluorescence pK_a value of 3.5 to the pK_a of 2.31 in 1:3 methanol:water 'Fluorescent indicator 1'. To confirm, measurements of **BODIPY 1** in a 1:3 methanol:water mixture are required.

3.3.3 Addition of BODIPY 1 to hydroxyapatite pellets

Our BODIPY dye was mixed with hydroxyapatite in one of three ways; **1)** suspension of hydroxyapatite powder in methanol, addition of a small amount of dye solution, followed by removal of solvent by rotary evaporation. **2)** Soaking a preformed pellet in a methanol solution containing dye for 30 minutes, removing the pellet from the solution and left to dry before storing. **3)** To a preformed pellet, 2-3 drops of dye dissolved in methanol were added and left to evaporate.

The first method provided the most uniform distribution of dye and would ensure in subsequent cell experiments, an osteoclast resorbing material would encounter dye in their acidic microenvironment no matter the depth of the pit. One limitation of this method is that if dye shows any fluorescence in the solid state, the UV light may penetrate past the first layer of hydroxyapatite to a layer that is not exposed to the solution and may not be in the off state. In experiments examining UV penetration of dentin in teeth, which also contains ~70% hydroxyapatite, penetration depths of ~100 μm were observed with excitation in the 455 – 495 nm range which we used.[20] This penetration depth is approximately 1/5 of the pellet thickness and given the hydroxyapatite grain size < 200 nm in samples made using materials from Sigma-Aldrich, excitation of dye molecules under the surface layer is possible.

Fluorescent imaging of pellets with dye applied using this method showed fluorescence in both acidic and basic conditions, summarized in **Table 4**. This observation prompted investigation into alternate dispersion techniques. The decreased fluorescence intensity at 10^{-2} M compared to the lower concentration of 10^{-5} M is likely a result of self-quenching.[21, 22]

Table 4. Average fluorescence intensity of hydroxyapatite pellets containing **BODIPY 1** dispersed evenly throughout the pellet.

Dye concentration (M)	pH 4.3	pH 7.5
0	264	268
10^{-2}	1632	1303
10^{-5}	1912	1843

The second method, submerging the pellet in dye-containing solution, is limited in usefulness as it is not possible to tell how much dye remains on the pellet. Using a dye more similar to pHocas-1 synthesized by Maeda *et al*, 2016 with bisphosphonate side chains would likely be more viable with this method of application due to the dye's affinity for hydroxyapatite.[7] Submerging the pellet

in dye-containing solution resulted in an uneven spread of dye on the pellet during evaporation and used too much dye per sample to be economical.

The third method, addition of 2-3 drops of dye-containing solution, was a more economical use of material, but still resulted in an uneven spread of dye on the surface of the pellet during evaporation.

Methods two and three where the pellet was surface coated would be potentially limited in usefulness to the early stages of resorption. As the resorption pit deepens, and osteoclast expels the dye into the media to be quenched along with the calcium and phosphate ions, no new dye would be exposed to the acidic microenvironment and fluorescence would halt.

3.3.4 Fluorescence imaging of hydroxyapatite pellets

Preliminary fluorescent imaging of hydroxyapatite controls excited between 455-495 nm showed an emission signal between 505-555 nm. This is same range in which **BODIPY 1** excites. While the average of the control intensity was 5-7 times smaller compared to dye-containing pellets, shown in **Table 4**, correlation of fluorescence intensity to pH osteoclast microenvironment during resorption would be more complicated due to the need to account for the fluorescence of the control. This problem amplified during our incorporation of collagen. As mentioned in **2.3.2**, incorporation of collagen into a hydroxyapatite pellet, while useful in making our samples more biomimetic and robust, further complicated the fluorescence as collagen also excites between 455-495 nm and emits between 505-555 nm. Collagen fluorescence is intense and accounts for approximately 2/3 of the fluorescence of whole bone.[23] In our experiments, incorporation of collagen resulted in clear areas of high fluorescence intensity, shown in **Figure 10**, in areas of high

collagen density. Maeda *et al*, 2016 circumvent these problems by use of two-photon excitation, to which we did not have easy access.[7, 23] Because of the increased intensity and heterogeneity, subsequent samples were made without the incorporation of collagen.

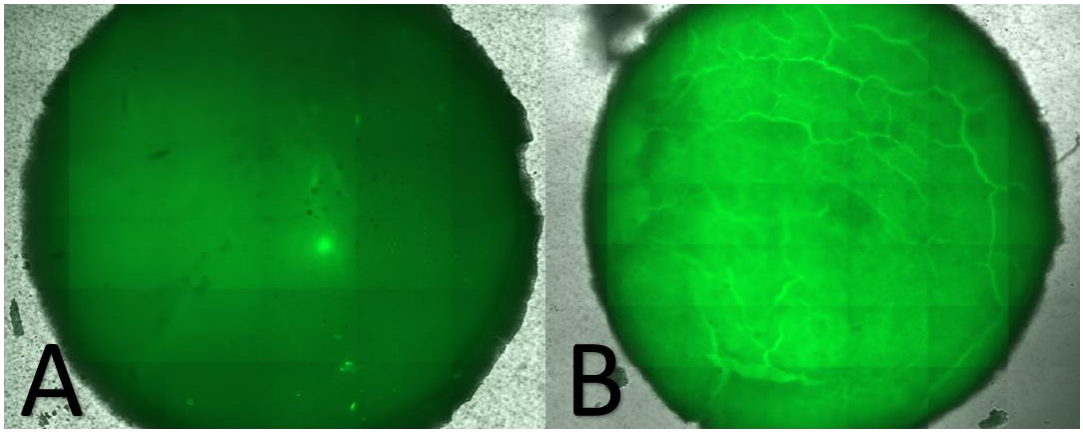

Figure 10. Fluorescence imaging of hydroxyapatite pellets. **A**) Hydroxyapatite **B)** 70:30 hydroxyapatite:collagen. Images are tiled composites where each tile is at 20x. The entire pellet is 8 mm in diameter.

The second problem to arise was fluorescence of dye-containing samples in neutral and basic conditions. Summarized in **Table 4**, samples in acid (pH 4.3) show higher average fluorescence counts of 1632 and 1912 at 10^{-2} M and 10^{-5} M, respectively. At slightly basic conditions, pH 7.5, average counts of 1303 and 1843 at 10^{-2} M and 10^{-5} M, respectively were observed. From our emission measurements shown **Figure 8**, we know at pH 7.5, our BODIPY should show minimal fluorescence. Intensities 5-7 times higher than controls at pH 7.5 indicate that the dye is not being adequately quenched. This could be due to penetration of light up to 100 μm into the pellet, past the top layer of hydroxyapatite, exciting the underlying dye molecules, where the solvent is unable to penetrate and quench the fluorescence.[20] This could explain why we only observe a 20-25% reduction in fluorescence intensity from pH 4.3 to pH 7.5.

In order to investigate the fluorescence of underlying layers we would need to surface coat a glass slide and observe firstly, if the dye is fluorescent is the solid state with no solution present, followed by experiments in acidic and neutral solutions, comparing the relative results to the observations made on the pellets.

Intensity levels in dye-containing samples are highest in acidic solutions, demonstrating that the dye does work as intended. As many of our experiments in acid took place at ~pH 4, relatively close to the pK_a, it is likely lowering the pH would result in even greater fluorescence intensities.

Due to the fluorescence of both the materials making up the pellets and the non-zero fluorescence observed from the dye when containing samples in neutral solution we decided to focus our efforts elsewhere. While we speculate it would be possible to subtract the average fluorescence intensity seen under basic conditions, setting as a baseline, the associated errors and increasing complexity required to correlate pH during osteoclast resorption to fluorescence intensity does not meet our goal of making a simple binary system.

3.3.5 Effects of hydroxyapatite sintering

Hydroxyapatite is often sintered to increase crystallinity, often to determine successful doping of the material with other elements such as Mg, Zn, Y, and Eu.[24-26] After sintering, hydroxyapatite acquires a blue colour, often attributed to trace contamination of manganese, a result we see in samples acquired from Sigma-Aldrich as well as hydroxyapatite synthesized in-house.[23]

Serendipitously, during fluorescence measurements we found that the average fluorescence count of hydroxyapatite samples that had been sintered was noted to be significantly lower compared to

their non-sintered counterparts, an example is shown in **Figure 11** and summary of results in **Table 5**.

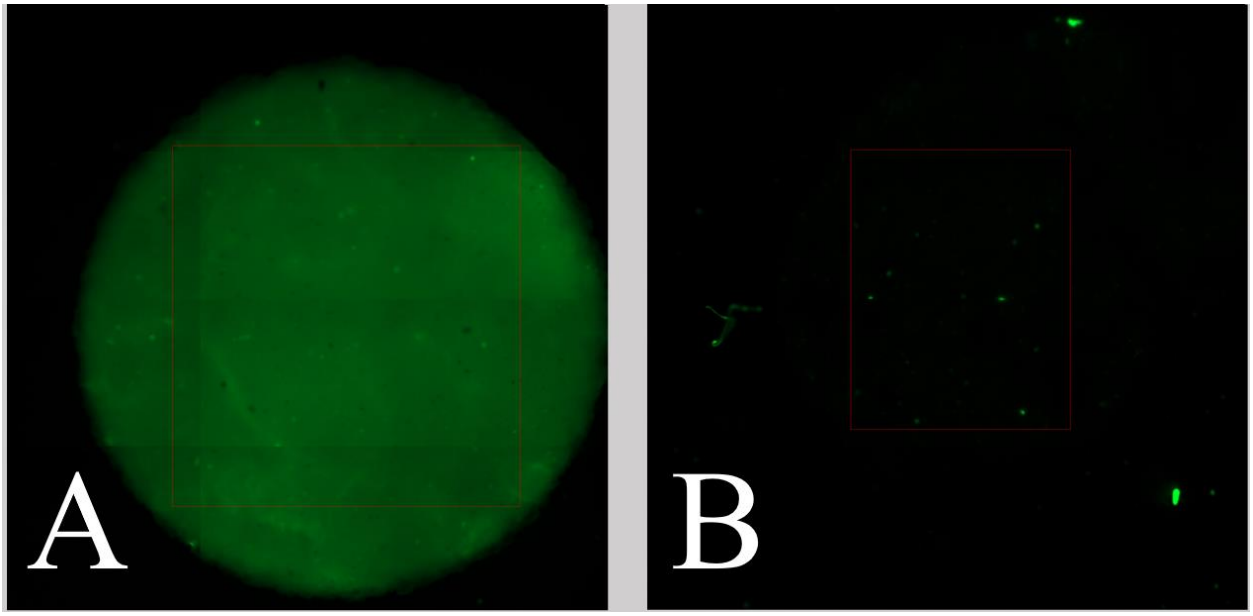

Figure 11. Fluorescence imaging of 1000 ppm tungsten doped hydroxyapatite **A)** non-sintered **B)** sintered at 1250°C for 8h. Images are tiled composites where each tile is at 20x. The entire pellet is 8 mm in diameter. 500 ms exposure time. Red rectangles indicate measured to determine average fluorescence count.

Table 5. Average fluorescence counts of tungsten doped hydroxyapatite at various concentrations comparing sintered and non-sintered variants. Values are rounded to the closest whole number. A background reading with no sample of 330 was subtracted from all values. An exposure time of 500 ms was used.

Conditions	0 ppm W-HAp	500 ppm W-HAp	1000 ppm W-HAp	10,000 ppm W-HAp
Non-sintered	240	250	508	103
Sintered at 1250°C	17	13	2	-2

Areas of high intensity in **Figure 11B** are suspected to be dust and other contaminants. Similar features are observed in **Figure 11A**, albeit less obvious due to the higher average intensity. In the production of future pellets for fluorescent imaging, additional care should be considered to reduce possible contaminants. More importantly, these results suggested that sintered hydroxyapatite does

not fluoresce like its non-sintered counterpart. This finding reignited the possibility of using our pH sensitive dye as the background signal of the sintered hydroxyapatite would be negligible.

We speculate that in hydroxyapatite synthesis, defect structures in the crystal are relatively common and that is largely responsible for the florescence. Ohzono *et al*. reports defects in liquid crystals result in areas of increased fluorescence intensity.[27] Another study reportedly increased fluorescence of nanocrystals by introducing defects, a feature that has been well documented in ZnO.[28, 29] If the frequency of defect structures is common enough in hydroxyapatite, the result could make the entire sample appear to fluoresce.

Subsequent efforts to reproduce these results were unsuccessful. One study attributes the observed fluorescence in hydroxyapatite to crystal shape, where thin rods show the highest intensities and spheres show no fluorescence.[30] This observation could account for our observations in the variability of fluorescence intensity, where one synthesis of hydroxyapatite results in rods and another spheres. One study on the effects of sintering of hydroxyapatite show relative density increasing as temperatures increase, up to 1250 °C. Scanning electron microscope images of the sintered powder from 1000 °C to 1250 °C in 50 °C increments show high porosity between crystals at 1000 °C decreasing with temperature where 1250 °C above show almost no gaps.[31] Hydroxyapatite before sintering has a low degree of crystallinity, showing very broad peaks in powder x-ray diffraction, with sharp peaks forming after sintering at temperatures of ≥1000 °C.[32]

Whether hydroxyapatite fluorescence is determined by morphology or the frequency of crystal defects or combination of the two, we believe sintering can reduce observed fluorescence. It is also likely that sintering time and temperature play an important role in these observations and needs to be fine-tuned in future studies for optimal results.

When sintered hydroxyapatite is pressed into an 8 mm pellet, the pellet does not hold its shape and is likely to crumble during its time in cell media and during handling. To solve this problem a binding agent replacement for collagen that does not fluoresce, does not readily dissolve in aqueous solution, and does not interact with osteoclast function is required.

3.3.6 Europium hydroxyapatite

Our most recent endeavor was to synthesize europium-doped hydroxyapatite, as another means for visualizing osteoclast activity. Europium (III) salts are commonly used fluorescent materials with applications from lamps to currency.[25] Europium (II) excites in the 370-400 nm range and emits from 410-500 nm while Europium (III) excites strongly at 395 nm and 465 nm and emits strongly at 590 nm and 612 nm.[25, 33] Our intention was to synthesize Eu hydroxyapatite, following the same procedure as W-doped hydroxyapatite outlined in **2.3.6** and examine the oxidation state of the europium using solid state fluorescence and XPS. Ideally for our application Eu(II) would be the dominant species. In the event the europium was Eu(III), as is suggested by similar synthesis, we would try the reduction of the sample to the 2+ state, performing follow up experiments to determine if the reduction degraded hydroxyapatite.[25, 34] In the event that Eu(II) hydroxyapatite is not easily achievable, we would resort to physical mixing of a Eu(II) salt with hydroxyapatite.

In changing our fluorescent molecule of interest from **BODIPY 1** to Eu(III) we would change the emission wavelength of interest to ~600 nm circumventing the problem of having additional sources of fluorescence at ~500 nm from hydroxyapatite and collagen allowing integration of collagen and use of pellets that are more biomimetic.[35] With Eu(II) as the dominant europium

species, we would be able to follow the oxidation of Eu(II) to Eu(III) mediated by osteoclast acidification *in vitro* without the use of two-photon excitation.

Eu hydroxyapatite at various concentrations has been demonstrated to have no negative impact on osteoblast proliferation.[34] If these results can be extrapolated to osteoclasts, see future work **4.2.4,** we would proceed with addition of Eu^{2+} to a sample seeded with osteoclasts to visualize the acidic microenvironment made by the osteoclast, giving a new method to visualize osteoclasts *in vivo* without inducing cell death.

3.4 Conclusion

We have synthesized and fully characterized a new BODIPY dye. While the dye was shown to be functional, it overlaps with strong natural bone emission, thus limiting its utility of *in vitro* visualization of osteoclast resorption of bonelike material. Sintering of hydroxyapatite has been shown to be a promising route to mitigation of observed fluorescence with further investigation on sintering conditions required. Work on synthesis and application of europium-doped hydroxyapatite as a means of visualization of *in vitro* osteoclast activity may prove to be useful.

3.5 References

1. Hayman, A. R.; Jones, S. J.; Boyde, A.; Foster, D.; Colledge, W. H.; Carlton, M. B.; Evans, M. J.; Cox, T. M., Mice lacking tartrate-resistant acid phosphatase (Acp 5) have disrupted endochondral ossification and mild osteopetrosis. *Development* **1996,** *122* (10), 3151-62.
2. Detsch, R.; Boccaccini, A. R., The role of osteoclasts in bone tissue engineering. *Journal of Tissue Engineering and Regenerative Medicine* **2015,** *9* (10), 1133-1149.
3. Hayman, A. R., Tartrate-resistant acid phosphatase (TRAP) and the osteoclast/immune cell dichotomy. *Autoimmunity* **2008,** *41* (3), 218-223.
4. Rodan, G. A.; Martin, T. J., Therapeutic Approaches to Bone Diseases. *Science* **2000,** *289* (5484), 1508.
5. Kowada, T.; Kikuta, J.; Kubo, A.; Ishii, M.; Maeda, H.; Mizukami, S.; Kikuchi, K., In Vivo Fluorescence Imaging of Bone-Resorbing Osteoclasts. *Journal of the American Chemical Society* **2011,** *133* (44), 17772-17776.
6. Kozloff, K. M.; Quinti, L.; Patntirapong, S.; Hauschka, P. V.; Tung, C.-H.; Weissleder, R.; Mahmood, U., Non-invasive optical detection of cathepsin K-mediated fluorescence reveals osteoclast activity in vitro and in vivo. *Bone* **2009,** *44* (2), 190-198.
7. Maeda, H.; Kowada, T.; Kikuta, J.; Furuya, M.; Shirazaki, M.; Mizukami, S.; Ishii, M.; Kikuchi, K., Real-time intravital imaging of pH variation associated with osteoclast activity. *Nature Chemical Biology* **2016,** *12* (8), 579-585.
8. Cavani, F., Heteropolycompound-based catalysts:: A blend of acid and oxidizing properties. *Catalysis Today* **1998,** *41* (1), 73-86.
9. Weinstock, I. A.; Cowan, J. J.; Barbuzzi, E. M. G.; Zeng, H.; Hill, C. L., Equilibria between α and β Isomers of Keggin Heteropolytungstates. *Journal of the American Chemical Society* **1999,** *121* (19), 4608-4617.
10. Hervé, G.; Tézé, A.; Contant, R., General Principles of The Synthesis of Polyoxometalates in Aqueous Solution. In *Polyoxometalate Molecular Science*, Borrás-Almenar, J. J.; Coronado, E.; Müller, A.; Pope, M., Eds. Springer Netherlands: Dordrecht, 2003; pp 33-54.
11. Strigul, N., Does speciation matter for tungsten ecotoxicology? *Ecotoxicology and Environmental Safety* **2010,** *73* (6), 1099-1113.
12. Boens, N.; Leen, V.; Dehaen, W., Fluorescent indicators based on BODIPY. *Chemical Society Reviews* **2012,** *41* (3), 1130-1172.
13. Werner, T.; Huber, C.; Heinl, S.; Kollmannsberger, M.; Daub, J.; Wolfbeis, O. S., Novel optical pH-sensor based on a boradiaza-indacene derivative. *Fresenius' Journal of Analytical Chemistry* **1997,** *359* (2), 150-154.
14. Sheldrick, G., Ashort history of SHELX. *Acta Crystallogr. A* **2008,** *64*, 112-122.
15. Sheldrick, G., SADABS: software for empirical absorption correction. *University of Gottingen, Institut fur Anorganische Chemieder Universitat, Tammanstrasse* **1996,** *4*, 1999-2003.
16. Toja, E.; Selva, D.; Schiatti, P., 3-Alkyl-2-aryl-3H-naphth[1,2-d]imidazoles, a novel class of nonacidic antiinflammatory agents. *Journal of Medicinal Chemistry* **1984,** *27* (5), 610-616.
17. Aldabbagh, F., 3.03 - Aldehydes: Aryl and Heteroaryl Aldehydes. In *Comprehensive Organic Functional Group Transformations II*, Katritzky, A. R.; Taylor, R. J. K., Eds. Elsevier: Oxford, 2005; pp 99-133.
18. Reijenga, J.; van Hoof, A.; van Loon, A.; Teunissen, B., Development of Methods for the Determination of pKa Values. *Anal Chem Insights* **2013,** *8*, 53-71.

19. Rived, F.; Canals, I.; Bosch, E.; Rosés, M., Acidity in methanol–water. *Analytica Chimica Acta* **2001,** *439* (2), 315-333.
20. Sholom, S.; Desrosiers, M.; Chumak, V.; Luckyanov, N.; Simon, S. L.; Bouville, A., UV effects in tooth enamel and their possible application in EPR dosimetry with front teeth. *Health Phys* **2010,** *98* (2), 360-368.
21. Zhegalova, N. G.; He, S.; Zhou, H.; Kim, D. M.; Berezin, M. Y., Minimization of self-quenching fluorescence on dyes conjugated to biomolecules with multiple labeling sites via asymmetrically charged NIR fluorophores. *Contrast Media Mol Imaging* **2014,** *9* (5), 355-362.
22. Chen, W.; Young, L. J.; Lu, M.; Zaccone, A.; Ströhl, F.; Yu, N.; Kaminski Schierle, G. S.; Kaminski, C. F., Fluorescence Self-Quenching from Reporter Dyes Informs on the Structural Properties of Amyloid Clusters Formed in Vitro and in Cells. *Nano Lett* **2017,** *17* (1), 143-149.
23. Bachman, C. H.; Ellis, E. H., Fluorescence of Bone. *Nature* **1965,** *206* (4991), 1328-1331.
24. Evis, Z.; Webster, T. J., Nanosize hydroxyapatite: doping with various ions. *Advances in Applied Ceramics* **2011,** *110* (5), 311-321.
25. Ciobanu, C. S.; Iconaru, S. L.; Massuyeau, F.; Constantin, L. V.; Costescu, A.; Predoi, D., Synthesis, Structure, and Luminescent Properties of Europium-Doped Hydroxyapatite Nanocrystalline Powders. *Journal of Nanomaterials* **2012,** *2012*, 942801.
26. Webster, T. J.; Massa-Schlueter, E. A.; Smith, J. L.; Slamovich, E. B., Osteoblast response to hydroxyapatite doped with divalent and trivalent cations. *Biomaterials* **2004,** *25* (11), 2111-2121.
27. Ohzono, T.; Katoh, K.; Fukuda, J.-i., Fluorescence microscopy reveals molecular localisation at line defects in nematic liquid crystals. *Scientific Reports* **2016,** *6* (1), 36477.
28. Uehara, M.; Watanabe, K.; Tajiri, Y.; Nakamura, H.; Maeda, H., Synthesis of CuInS2 fluorescent nanocrystals and enhancement of fluorescence by controlling crystal defect. *The Journal of Chemical Physics* **2008,** *129* (13), 134709.
29. Zhou, J.; Nomenyo, K.; Cesar, C. C.; Lusson, A.; Schwartzberg, A.; Yen, C.-C.; Woon, W.-Y.; Lerondel, G., Giant defect emission enhancement from ZnO nanowires through desulfurization process. *Scientific Reports* **2020,** *10* (1), 4237.
30. Deshmukh, K.; Shaik, M. M.; Ramanan, S.; Kowshik, M., Self-Activated Fluorescent Hydroxyapatite Nanoparticles: A Promising Agent for Bioimaging and Biolabeling. *ACS Biomaterials Science & Engineering* **2016,** *2*.
31. Muralithran, G.; Ramesh, S., The effects of sintering temperature on the properties of hydroxyapatite. *Ceramics International* **2000,** *26* (2), 221-230.
32. Indrani, D.; Soegijono, B.; Adi, W.; Trout, N., Phase composition and crystallinity of hydroxyapatite with various heat treatment temperatures. *International Journal of Applied Pharmaceutics* **2018,** *9*, 87.
33. Herrmann, A.; Fibikar, S.; Ehrt, D., Time-resolved fluorescence measurements on Eu3+- and Eu2+-doped glasses. *Journal of Non-Crystalline Solids* **2009,** *355* (43), 2093-2101.
34. Frumosu, F.; Iconaru, S. L.; Predoi, D., Europium concentration effect of europium doped hydroxyapatite on proliferation of osteoblast cells. *Digest Journal of Nanomaterials and Biostructures* **2011,** *6*, 1859-1865.
35. Binnemans, K.; Lenaerts, P.; Driesen, K.; Görller-Walrand, C., A luminescent tris(2-thenoyltrifluoroacetonato)europium(iii) complex covalently linked to a 1,10-phenanthroline-functionalised sol–gel glass. *Journal of Materials Chemistry* **2004,** *14* (2), 191-195.

Chapter 4

Conclusions and Future Work

4.1 Conclusions

Herein we have presented a procedure for hydroxyapatite pellet formation for use as a biomimetic substate for *in vitro* osteoclast study. We have incorporated collagen into the matrix by physical means making the pellet more robust and biomimetic. Tungsten-containing compounds have been incorporated into the hydroxyapatite pellets by physical means and tungsten-doped hydroxyapatite has been synthesized by precipitation of hydroxyapatite in the presence of dissolved tungsten. Tungsten XANES spectra of tungsten-doped hydroxyapatite most closely resembles the spectrum of sodium tungstate. Using laser ICP-MS and 2D XRF we have demonstrated tungsten is most uniformly dispersed in tungsten-doped hydroxyapatite and there is no significant difference in dispersion in the physical mixing methods of mechanical grinding with a pestle and mortar, mixing in water with stirring, or mixing in water using an ultra-sonication horn. Using 2D XRF we have

obtained maps of osteoclasts and their resorption pits. Tungsten XANES spectra acquired at several locations of a hydroxyapatite pellet seeded with osteoclasts show predominantly one species of tungsten, with a few scans showing the emergence of a secondary peak, suggesting acidic microenvironment made by osteoclasts could be responsible for conversion of tungsten species. Additionally, we have synthesized and fully characterized a new pH sensitive BODIPY dye designed to fluoresce under the acidic conditions of a resorbing osteoclast while quenched under physiological conditions. We have demonstrated the function of BODIPY 1, however its absorbance maxima of 499 nm and fluorescence emission at 510 nm overlaps with the natural emissions of hydroxyapatite and collagen, limiting its utility for *in vitro* visualization of osteoclast resorption of bonelike material.

4.2 Future work

The future of this work lies in the validation of our assumptions, replication of results, and optimization of experimental conditions. Many of the experiments presented herein have the potential for further study in the form of either subsequent experiments to confirm our findings, or to use our findings as a foundation for novel experiments.

4.2.1 Loading efficiency of tungsten in tungsten-doped hydroxyapatite

A key assumption we made was 100% integration of tungsten in tungsten-doped hydroxyapatite. In the event this is not the case, tungsten-doped hydroxyapatite at a given concentration would not be directly comparable to physical mixtures of tungsten compounds and hydroxyapatite due to the discrepancies in total tungsten concentration. To test the loading efficiency of tungsten in tungsten-

doped hydroxyapatite we would use x-ray photoelectron spectroscopy (XPS). Sodium tungstate mixed with hydroxyapatite of known tungsten concentrations would be used as controls. In duplicate, we would synthesize tungsten-doped hydroxyapatite by precipitation as described in **2.3.6** with a replicate where the sodium tungstate is added to the calcium hydroxide prior to precipitation to test if the order of addition changes the loading. The tungsten signal intensity in the XPS spectra in tungsten-doped hydroxyapatite would be plotted against the control. Tungsten concentrations would be increased until the tungsten signal in tungsten-doped hydroxyapatite no longer increased and the resulting plot of synthetic vs control would be used as a calibration curve for subsequent syntheses.

4.2.2 Use of XANES to study the conversion of tungsten speciation by osteoclast activity

As we were unable to select the area of study and acquire light microscope images of the scanned area due to travel restrictions our results were based on this experiment alone. It has been shown in previous experiments that there is a change in tungsten speciation in bone, but our results are the first to suggest that the change is a result of osteoclast activity.[1] This finding is important and it is of utmost importance that these experiments be continued. As there is the limitation that during the one-week incubation period, osteoclasts are only able to convert a relatively small proportion of the total tungsten content, the following experimental changes would be investigated independently and together. First, we would experiment with sodium tungsten dissolved in cell media rather than dispersed through the pellet so the tungsten precipitated in the acidic microenvironment would be the only tungsten species present. Secondly, we would extend the incubation period to two weeks, and would investigate the viability of multiple rounds of seeding on one pellet in order to maximize the conversion of tungsten species.[2]

4.2.3 Sintering of hydroxyapatite to reduce background fluorescence

Based on our preliminary observations, sintered hydroxyapatite demonstrates reduced fluorescence. As mentioned in **3.4.5**, crystal shape and defect rate are likely to play a role in fluorescence.[3-5] Sintering of hydroxyapatite has been shown to increase density, decrease defect rate and control of shape.[6] Using the work by Muralithran *et al.* as a reference, we would extend their studies to include the effects of sintering time and temperature on the fluorescence of hydroxyapatite.[6] Elimination of the fluorescence of hydroxyapatite would provide the binary system for visualization of osteoclast resorption we aimed to achieve in use of BODIPY 1.

To address the fluorescence of collagen and the tendency for sintered hydroxyapatite pellets to crumble, a non-fluorescent binder would be required. One such example that has found success in x-ray fluorescence measurements is Polyvinylpyrrolidone-methylcellulose.[7] Testing would need to be conducted on any potential binder to ensure it does not impact osteoclast development or function.

4.2.4 Effect of europium on osteoclast proliferation

Frumosu *et al.* demonstrated in 2011 that europium-doped hydroxyapatite had no negative impacts on osteoblasts.[8] It would be worthwhile to expand on their experiments to show the presence of Eu does not negatively impact osteoclasts, as osteoblasts are responsible for producing and placing new material, and likely not interacting directly with Eu, whereas osteoclasts resorb material, releasing Eu into solution and potentially resulting in cellular uptake.

4.3 References

1. VanderSchee, C. R.; Kuter, D.; Bolt, A. M.; Lo, F.-C.; Feng, R.; Thieme, J.; Chen-Wiegart, Y.-c. K.; Williams, G.; Mann, K. K.; Bohle, D. S., Accumulation of persistent tungsten in bone as in situ generated polytungstate. *Communications Chemistry* **2018,** *1* (1), 8.
2. Manolagas, S. C., Birth and Death of Bone Cells: Basic Regulatory Mechanisms and Implications for the Pathogenesis and Treatment of Osteoporosis*. *Endocrine Reviews* **2000,** *21* (2), 115-137.
3. Ohzono, T.; Katoh, K.; Fukuda, J.-i., Fluorescence microscopy reveals molecular localisation at line defects in nematic liquid crystals. *Scientific Reports* **2016,** *6* (1), 36477.
4. Uehara, M.; Watanabe, K.; Tajiri, Y.; Nakamura, H.; Maeda, H., Synthesis of CuInS2 fluorescent nanocrystals and enhancement of fluorescence by controlling crystal defect. *The Journal of Chemical Physics* **2008,** *129* (13), 134709.
5. Deshmukh, K.; Shaik, M. M.; Ramanan, S.; Kowshik, M., Self-Activated Fluorescent Hydroxyapatite Nanoparticles: A Promising Agent for Bioimaging and Biolabeling. *ACS Biomaterials Science & Engineering* **2016,** *2*.
6. Muralithran, G.; Ramesh, S., The effects of sintering temperature on the properties of hydroxyapatite. *Ceramics International* **2000,** *26* (2), 221-230.
7. Watson, J. S., Fast, Simple Method of Powder Pellet Preparation for X-Ray Fluorescence Analysis. *X-Ray Spectrometry* **1996,** *25* (4), 173-174.
8. Frumosu, F.; Iconaru, S. L.; Predoi, D., Europium concentration effect of europium doped hydroxyapatite on proliferation of osteoblast cells. *Digest Journal of Nanomaterials and Biostructures* **2011,** *6*, 1859-1865.

Supplemental figures

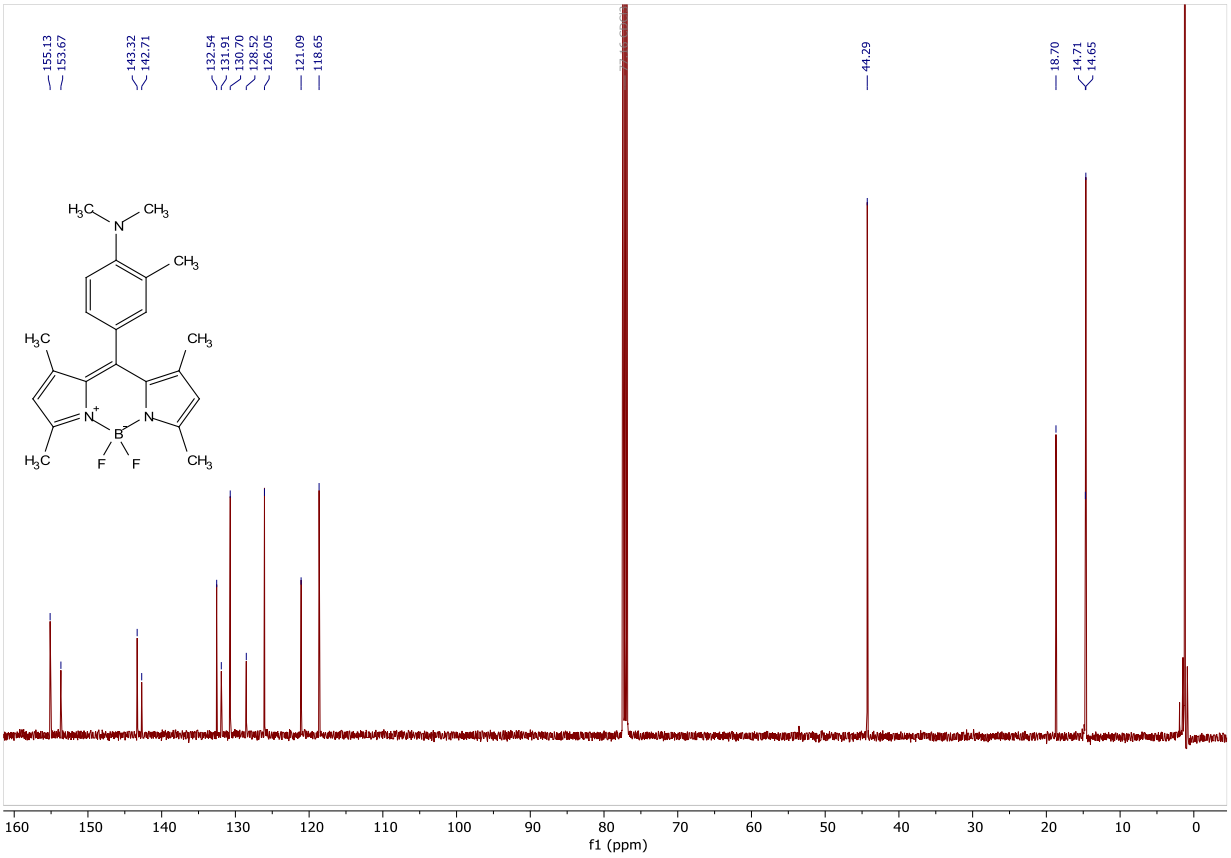

Supplemental figure 1. BODIPY 1 ^{13}C NMR ($CDCl_3$, 125.81 MHz): δ 155.1, 153.7, 143.3, 143.3, 142.7, 132.5, 131.9, 130.7, 128.5, 126.1, 121.1, 118.7, 44.3, 18.7, 14.7, 14.7.

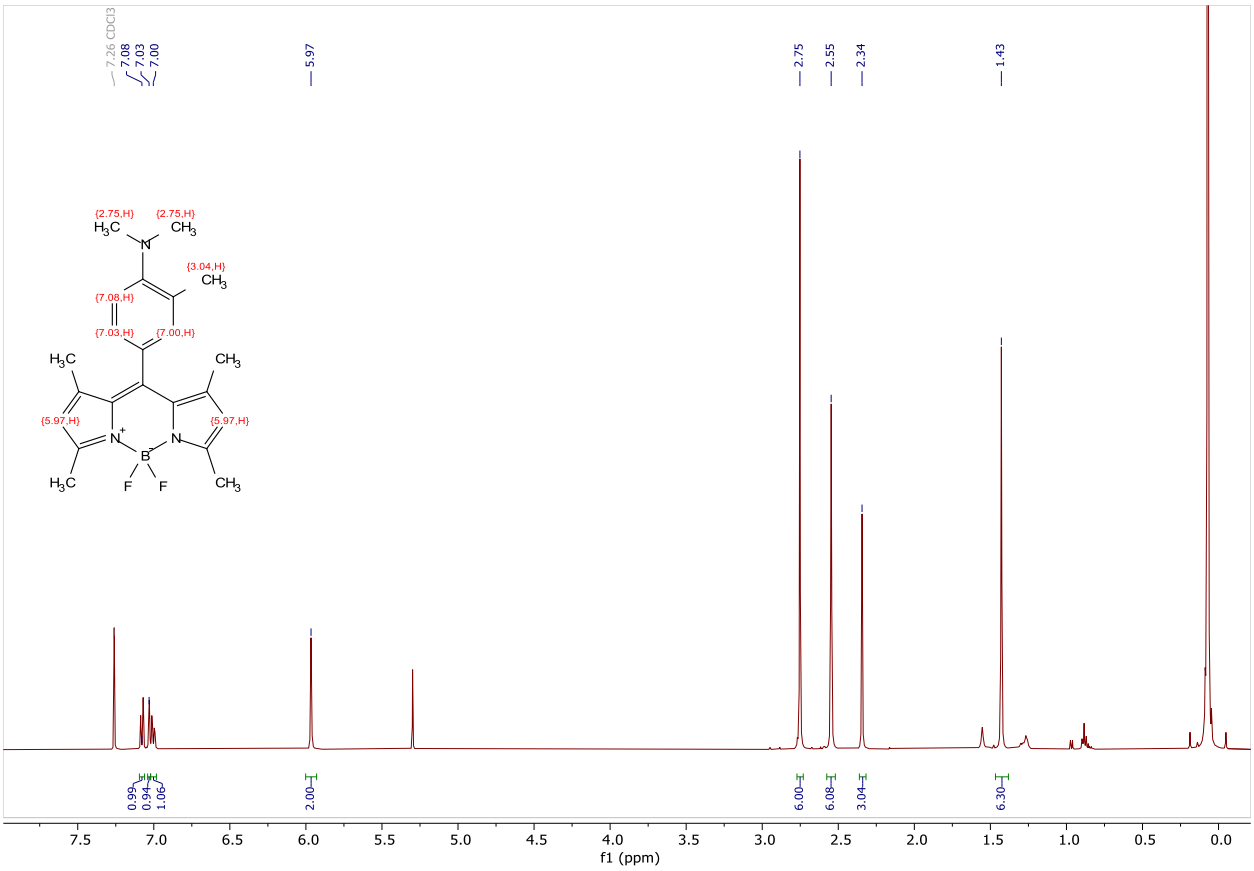

Supplemental figure 2. BODIPY 1 ^{1}H NMR ($CDCl_3$, 500.30 MHz): δ 7.08 (m, 1H), 7.03 (m, 1H), 7.00 (m, 1H), 2.75 (s, 6H), 2.55 (s, 6H), 2.34 (s, 3H), 1.43 (s, 6H).

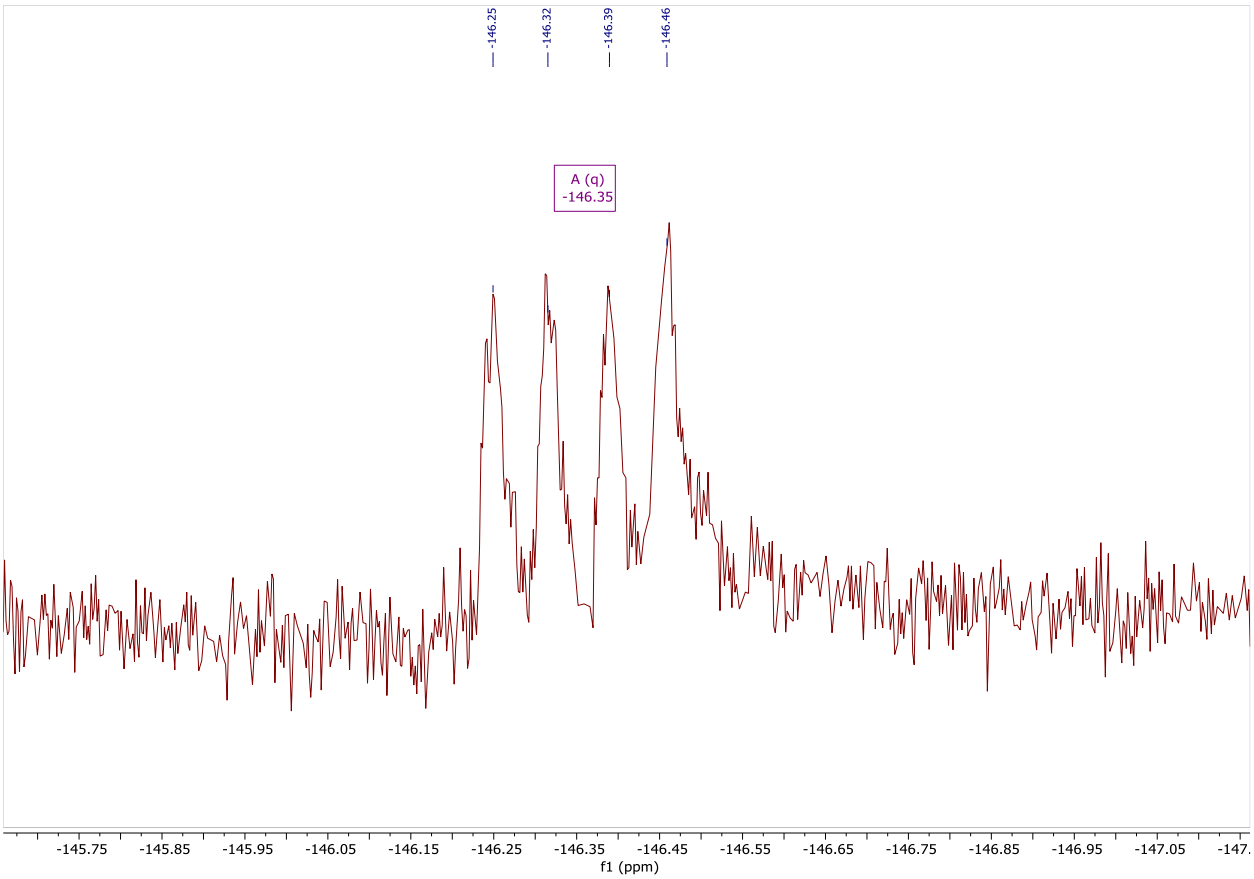

Supplemental figure 3. BODIPY 1 ^{19}F NMR ($CDCl_3$, 470.71 MHz): δ 146.35 (q, J = 32.9 Hz).

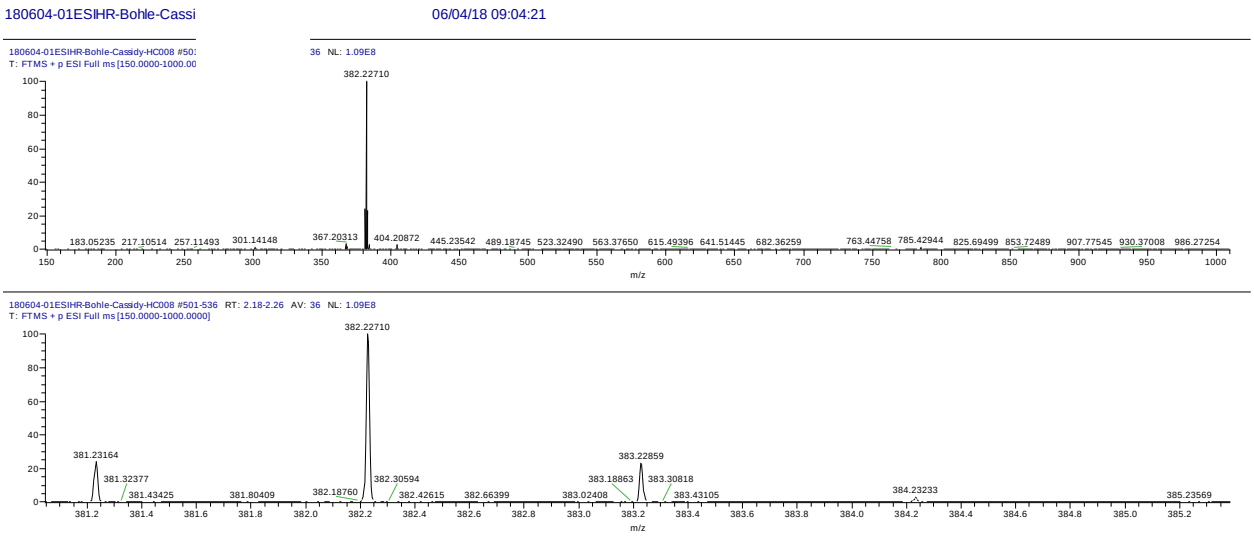

180604-01ESIHR-Bohle-Cassidy-HC008#501-536 RT: 2.18-2.26 AV: 36
T: FTMS + p ESI Full ms [150.0000-1000.0000]
m/z= 382.21515-382.26744

m/z	Intensity	Relative	Resolution	Charge	Theo. Mass	Delta (ppm)	RDB equiv.	Composition
382.22710	111434904.0	100.00	26901.75	1.00	382.22606	2.72	10.5	$C_{22}H_{27}N_3BF_2$
					382.22892	-4.76	10.5	$C_{23}H_{29}ON_3F$

Supplemental figure 4. BODIPY 1 ESI$^+$-MS.

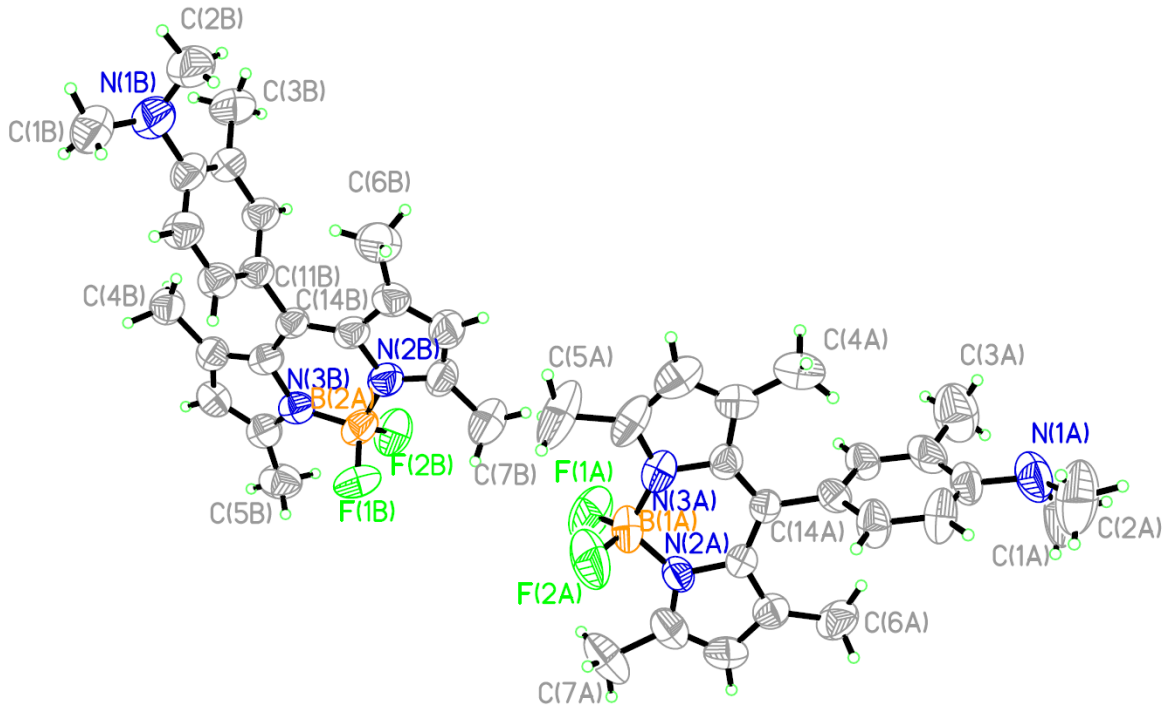

Supplemental figure 5. BODIPY 1 crystal structure.

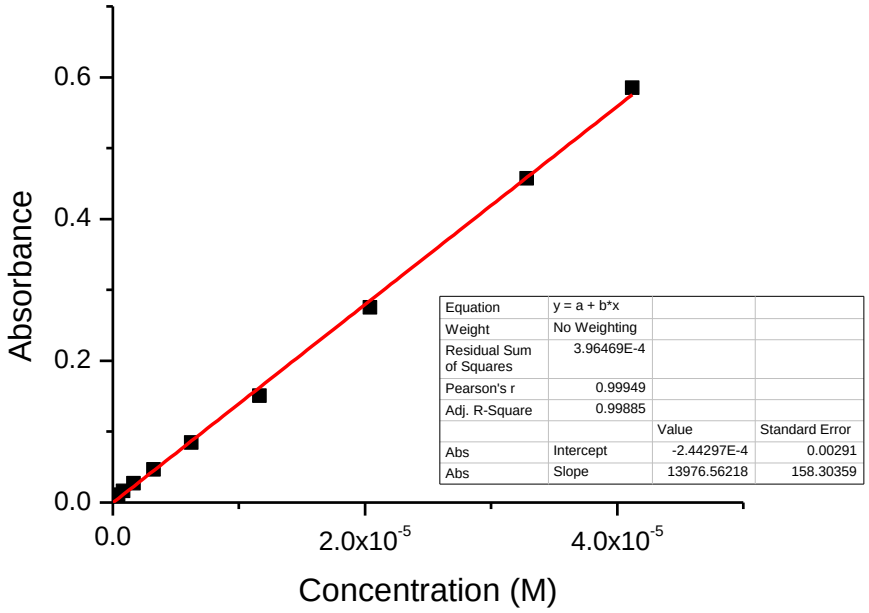

Supplemental figure 6. UV-vis plot of absorbance vs concentration of **BODIPY 1** in MeOH at λ 499 nm. Extinction coefficient (ε) is 14,000.